



Model-based learning for multi-antenna multi-frequency location-to-channel mapping

Baptiste Chatelier, Vincent Corlay, Matthieu Crussière, Luc Le Magoarou

► To cite this version:

Baptiste Chatelier, Vincent Corlay, Matthieu Crussière, Luc Le Magoarou. Model-based learning for multi-antenna multi-frequency location-to-channel mapping. 2024. hal-04612749v2

HAL Id: hal-04612749

<https://hal.science/hal-04612749v2>

Preprint submitted on 8 Jul 2024

HAL is a multi-disciplinary open access archive for the deposit and dissemination of scientific research documents, whether they are published or not. The documents may come from teaching and research institutions in France or abroad, or from public or private research centers.

L'archive ouverte pluridisciplinaire **HAL**, est destinée au dépôt et à la diffusion de documents scientifiques de niveau recherche, publiés ou non, émanant des établissements d'enseignement et de recherche français ou étrangers, des laboratoires publics ou privés.

Model-based learning for multi-antenna multi-frequency location-to-channel mapping

Baptiste Chatelier, Vincent Corlay, Matthieu Crussière, Luc Le Magoarou

Abstract—Years of study of the propagation channel showed a close relation between a location and the associated communication channel response. The use of a neural network to learn the location-to-channel mapping can therefore be envisioned. The Implicit Neural Representation (INR) literature showed that classical neural architecture are biased towards learning low-frequency content, making the location-to-channel mapping learning a non-trivial problem. Indeed, it is well known that this mapping is a function rapidly varying with the location, on the order of the wavelength. This paper leverages the model-based machine learning paradigm to derive a problem-specific neural architecture from a propagation channel model. The resulting architecture efficiently overcomes the spectral-bias issue. It only learns low-frequency sparse correction terms activating a dictionary of high-frequency components. The proposed architecture is evaluated against classical INR architectures on realistic synthetic data, showing much better accuracy. Its mapping learning performance is explained based on the approximated channel model, highlighting the explainability of the model-based machine learning paradigm.

Index Terms—Model-based machine learning, Implicit Neural Representations, Spectral bias, Sparse representation, MIMO

I. INTRODUCTION

FOR the past decades, signal processing methods have been used to improve communication systems. Such methods are model-based: they can present a high bias but benefit from a reasonable complexity. With the emergence of easily accessible computational power, artificial intelligence (AI)/machine learning (ML) has emerged as a promising alternative to signal processing methods in many communication problems. By essence, AI/ML methods are data-based: they consequently present a low bias due to their intrinsic adaptability capabilities. However, the training prerequisites of such methods entail substantial computational and sample complexities. Recently, researchers have focused on bridging the gap between those two paradigms using a hybrid approach: model-based machine learning [1]. This approach proposes to use models from signal processing, to structure, initialize, and train learning methods from AI/ML. The underlying goal is to reduce the bias of signal processing methods by making models more flexible, while guiding AI/ML methods to reduce their complexity.

Baptiste Chatelier is with Mitsubishi Electric R&D Centre Europe, Univ Rennes, INSA Rennes, CNRS, IETR-UMR 6164 and b<>com, Rennes, France (email: baptiste.chatelier@insa-rennes.fr).

Vincent Corlay is with Mitsubishi Electric R&D Centre Europe and b<>com, Rennes, France (email: v.corlay@fr.mercede.mee.com).

Matthieu Crussière and Luc Le Magoarou are with Univ Rennes, INSA Rennes, CNRS, IETR-UMR 6164 and b<>com, Rennes, France (email: {matthieu.crussiere ; luc.le-magoarou}@insa-rennes.fr).

In the past few years, model-based machine learning have showed great results in channel estimation problems [2]–[5], angle of arrival estimation [6], channel charting [7]–[9], but also in integrated sensing and communication scenarios [10]. It is proposed to further explore this paradigm by studying the location-to-channel mapping learning: as the propagation channel coefficients are closely related to the user’s location, one can use a neural network to learn this specific mapping. Upon training completion, one only has to input a location to the neural network to acquire the channel coefficients at the given location. In order to do so, one can use a physical propagation model to derive a model-based (MB) neural architecture specifically adapted for the location-to-channel mapping learning.

This approach would be beneficial in many applications: channel estimation, secure communication mechanisms, resource allocation, interference management, and also radio-environment compression. Indeed, if one achieves near perfect learning of the location-to-channel mapping, it could be more efficient to only store the weights of the trained neural network rather than directly storing the channel coefficients.

Learning continuous mappings with neural networks is known as the Implicit Neural Representation (INR) problem. After its great success in the resolution of image processing problems such as novel view synthesis [11], researchers have started to establish theoretical results on the INRs mapping learning capabilities [12]–[17]. While classical architectures, such as multi-layer perceptrons (MLPs), are universal function approximators [18], [19], it has been shown that they exhibit a bias towards learning low-frequency functions, a phenomenon known as spectral bias [20]–[22]. This makes classical architectures unsuitable for the learning of rapidly varying functions. To address this limitation, specialized architectures have been developed: random Fourier features (RFFs) [23], [24], sinusoidal representation networks (SIRENs) [25] or Gaussian activated radiance fields (GARFs) [26]. Theoretical results in [14] characterized the expression power of both RFFs and SIRENs: such architectures can only represent functions being linear combinations of specific harmonics of their input mapping. This demonstrates the high-frequency learning capability of those architectures. The location-to-channel mapping presents a high-frequency spatial dependence, on the order of the operating wavelength, making its learning a remarkably complex problem. One may then pose the subsequent inquiries: *Are classical INR architectures able to learn the location-to-channel mapping? Is a model-based approach able to learn this mapping? Does the model-based approach outperform INR architectures in*

terms of learning performance and complexity?

Contributions. It is proposed to leverage the capabilities of model-based machine learning for the location-to-channel mapping learning. To maintain generality, this mapping learning problem is examined over multiple antennas and multiple frequencies. The following contributions are presented in this paper:

- A theoretical study of a physics-based channel model, using Taylor expansions, allows to clearly separate low and high-frequency spatial contents (Lemma 1, Proposition 1, Proposition 2).
- A sparse signal processing approach, using sparse representations of the channel, is presented to ensure the validity of the obtained channel approximation across the entire \mathbb{R}^3 space (Theorem 1).
- A model-based neural architecture is derived from the approximated channel model. It is shown that the obtained structure shares common features with classical INR architectures, such as a spectral separation stage with a high-frequency embedding, allowing to bypass the spectral-bias issue.
- Experiments are conducted on realistic channels, showing the great potential of the proposed approach, both in terms of learning performance and computational efficiency. Moreover, some experiments clearly show that the proposed approach successfully learns the underlying physical models, enabling efficient generalization.

Related work. Learning continuous mappings through neural networks has been extensively studied by the image processing community. For instance, it has been used for image reconstruction problems [25], [27], [28], for 3D scene reconstruction from 2D images [11], [29], [30] but also for dynamic 3D scene reconstruction from 2D images [31]–[35]. In the signal processing community, machine learning capabilities have been recently leveraged for various problems: e.g. ML-based channel estimation [36]–[39]. There also exist works about mapping learning in communication problems: specifically, the location/pseudo-location-to-beamformer mapping learning has been studied in [40] and [41], as well as the pseudo-location-to-best-codebook-index mapping learning in [8]. Additionally, our previous work in [42] studied the location-to-channel mapping learning in a simplified scenario: only a single antenna and frequency were considered. In this paper, the scenario is extended to multiple antennas and multiple frequencies, making the proposed approach better suited to more realistic scenarios. In [43], the authors propose to adapt the neural radiance fields concept of [11] from optical to radio-frequency signals. However, the proposed model requires complex learning strategies and long training times. Additionally, the proposed model is used for downlink channel estimation in a frequency division duplex setting, but requires the uplink channel knowledge. In this paper, the proposed approach only requires the receiver location knowledge and possesses relatively low sample complexity. Finally, in [44], the authors proposed to calibrate electromagnetic properties of a scene, e.g. material permittivity and conductivity, scattering and reflection coefficients, using a differentiable ray-tracing approach. Upon completion of the

calibration process, accessing the scene properties in different configurations becomes feasible. Among other applications, using the calibrated scene enables the accurate computation of the propagation channel response at different locations, through ray-tracing. The primary distinction between this differentiable ray-tracing method and the suggested approach is that the former emphasizes on calibrating a specific scene at the electromagnetic property level while considering the scene topology known. Conversely, the latter proposes a straightforward approach for the continuous location-to-channel mapping learning using a model-based neural network with no prior information about the scene topology.

Organization. The rest of the paper is organized as follows. Section II properly presents the location-to-channel mapping learning problem, Section III exposes the classical INR approaches as well as the theoretical contributions. Then, Section IV presents the translation of the proposed model into a neural architecture. Section V proposes to evaluate the developed architecture against several baselines on realistic synthetic data. Finally, Section VI introduces some conclusions and perspectives for future work.

Notations. Lowercase bold letters represent vectors while uppercase bold letters represent matrices. \mathbb{R} and \mathbb{C} respectively denotes the real and complex fields. o denotes the small- o Bachman-Landau notation. \cdot^T denotes the transpose matrix operator. $\text{diag}(\cdot)$ denotes the matrix operator constructing a diagonal matrix from a vector and $\text{vec}(\cdot)$ denotes the vectorization operator. $\mathbf{Id}_N \in \mathbb{R}^{N \times N}$ denotes the identity matrix, while $\mathbf{0}_N \in \mathbb{R}^{N \times N}$ denotes the null matrix. \odot denotes the Hadamard product, and \otimes denotes the Kronecker product. $\nabla_{\mathbf{a}} f(\mathbf{a}, \mathbf{b})$ denotes the gradient operator wrt. \mathbf{a} . $|\cdot|$ denotes the absolute value for real numbers, modulus for complex numbers and cardinal for sets. $\|\cdot\|_p, p \in \mathbb{N}$ denotes the ℓ_p norm, and $\|\cdot\|_F$ denotes the ℓ_F (Frobenius) norm. \mathcal{S}_1 denotes the unit sphere while \mathcal{C}_1 denotes the unit circle. $\delta(t)$ denotes the Dirac impulse. $\Re\{\cdot\}$ and $\Im\{\cdot\}$ denotes the real and imaginary parts.

II. PROBLEM FORMULATION

In this section, the physical propagation channel model is presented, and the mapping-learning problem is defined.

Let us consider a communication system where a base station (BS) transmits information through N_a antennas and N_s distinct frequencies to mono-antenna user equipments (UEs). In the time domain, the propagation channel defines the filter operating on the electromagnetic waves transmitted between an emitting and receiving antenna. This filter impulse response is classically known as the channel impulse response (CIR). Considering the propagation channel over L_p specular propagation paths between the j th BS antenna and a mono-antenna receiver located at $\mathbf{x} \in \mathbb{R}^3$ yields the following CIR definition:

$$\bar{h}_j(t, \mathbf{x}) = \sum_{l=1}^{L_p} \alpha_l(\mathbf{x}) \delta(t - \tau_l(\mathbf{x})), \quad (1)$$

where $\alpha_l(\mathbf{x}) \in \mathbb{R}$, resp. $\tau_l(\mathbf{x}) \in \mathbb{R}$, is the attenuation coefficient, resp. propagation delay, for the l th path.

Applying the Fourier transform on the CIR yields the frequency channel response. For a given frequency f_k , this gives:

$$\begin{aligned} h_j(f_k, \mathbf{x}) &= \sum_{l=1}^{L_p} \alpha_l(\mathbf{x}) e^{-j2\pi f_k \tau_l(\mathbf{x})} \\ &= \sum_{l=1}^{L_p} \frac{\gamma_l}{d_l(\mathbf{x})} e^{-j\frac{2\pi}{\lambda_k} d_l(\mathbf{x})}, \end{aligned} \quad (2)$$

where $\lambda_k \triangleq c/f_k \in \mathbb{R}$ is the wavelength associated to frequency f_k and $d_l(\mathbf{x}) \in \mathbb{R}$ represents the propagation distance for the l th path. In further developments, the frequency dependence in Eq. (2) is dropped and the notation $h_{j,k}(\mathbf{x})$ is used. In Eq. (2), it is assumed that the attenuation is proportional to $d_l(\mathbf{x})$ and that the delay is such that:

$$\tau_l(\mathbf{x}) \triangleq \begin{cases} \frac{d_l(\mathbf{x})}{c}, l = 1 \\ \frac{d_l(\mathbf{x})}{c} - \nu_l, l \neq 1 \end{cases}, \quad (3)$$

where $\nu_l \in \mathbb{R}$ accounts for a supplementary delay induced by wave-matter interactions. As a result, the attenuation coefficient γ_l becomes complex: $\forall l > 1$, $\Re\{\gamma_l\}$ and $\Im\{\gamma_l\}$ represent the small-scale attenuation and phase shift introduced along the l th path. Note that $\Re\{\gamma_1\} = 1$ and $\Im\{\gamma_1\} = 0$ when considering a Line of Sight (LoS) path, as this path does not present any wave-matter interaction.

Then, using the virtual source theory [45, Chapter 1, pp.47-49] to model the propagation distance $d_l(\mathbf{x})$ yields:

$$h_{j,k}(\mathbf{x}) = \sum_{l=1}^{L_p} \frac{\gamma_l}{\|\mathbf{x} - \mathbf{a}_{l,j}\|_2} e^{-j\frac{2\pi}{\lambda_k} \|\mathbf{x} - \mathbf{a}_{l,j}\|_2}, \quad (4)$$

where $\mathbf{a}_{l,j} \in \mathbb{R}^3$ denotes the location of the l th virtual antenna, so that $1/\|\mathbf{x} - \mathbf{a}_{l,j}\|_2$ represents the large scale fading of the l th path.

Remark. Note that Eq. (4) models a multipath channel, where the L_p propagation paths are distinguishable paths: they can result from reflection, diffraction or scattering. Moreover, while the virtual source theory is classically used to model reflections, it can also accounts for diffraction [46].

The exponential argument in Eq. (4) reveals a high-frequency spatial dependence: a small change in the location \mathbf{x} induces a significant change in the channel coefficient $h_{j,k}(\mathbf{x})$. This arises from the wavelength dependence in the exponential argument: as the carrier frequency rises, the wavelength drops, yielding the fast variation of channel coefficients in the location space. In classical communication systems (sub-6GHz), λ is on the order of a few centimeters. 5G/6G systems also consider millimeter wavelengths.

Let $\mathbf{H}(\mathbf{x}) \in \mathbb{C}^{N_a \times N_s}$ be the antenna-frequency channel matrix at location \mathbf{x} . This matrix is constructed from the concatenation of the complex frequency-channel coefficients $h_{j,k}(\mathbf{x})$ in Eq. (4), across every antenna and frequency. The goal of this study is to learn:

$$\begin{aligned} f_{\theta}: \mathbb{R}^3 &\longrightarrow \mathbb{C}^{N_a \times N_s} \\ \mathbf{x} &\longrightarrow \mathbf{H}(\mathbf{x}), \end{aligned} \quad (5)$$

a neural network f parameterized by a set of learning parameters θ that learns the continuous mapping between a location \mathbf{x} and complex channel matrix $\mathbf{H}(\mathbf{x})$. As mentioned in the introduction, the high-frequency spatial dependency in the channel model causes the location-to-channel mapping to be remarkably hard to learn using classical neural architectures due to the spectral bias issue. Alternative neural architectures overcoming this issue are presented in the next section.

III. FROM CLASSICAL

INR ARCHITECTURES TO A MODEL-BASED APPROACH

This section first proposes a brief overview on the recent INR architecture evolution for the learning of rapidly varying functions. Then, the proposed model-based approach is presented, as well as the related theoretical results.

A. Classical INR architectures

Specific architectures have been developed in order to circumvent the spectral-bias limitation of classical neural architectures. This limitation occurs in some image processing applications: e.g. given a specific camera location and orientation, is it possible to use a neural network for the synthesis of views that have not been captured by the camera? As variations in pixel color and intensity contain high frequencies (e.g. on boundaries, in text ...), directly learning the orientation and location-to-view mapping is not a trivial task. It has been proposed in [11] to introduce a high-frequency embedding in the neural architecture, to ease the high-frequency content learning. This embedding has been known as a *positional embedding*: a given location or pseudo-location information (e.g. 5D coordinates from camera location and orientation) is projected into a higher dimensional space containing high frequencies. Such an approach is coherent with earlier work in [20], where authors showed that introducing a particular high-frequency embedding allowed to ease the learning of high-frequency content in the target mapping. Further work on the development of spectral-bias resistant neural architectures can be divided into two categories: embedding specialization in traditional ReLU-MLP and embedding replacement.

Embedding specialization. This approach consists in the design of a well adapted embedding layer for the target mapping learning, while the rest of the neural architecture is a traditional ReLU-MLP. This approach, known as positional embedding, has been used in [11], [24], [31], [32], [34].

Embedding replacement. On the other hand, this approach proposes to drop the initial high-frequency embedding and to specialize the activation functions of the MLP. This recently gained a lot of interest: in [25], authors proposed to replace ReLU non-linearities by sine functions, achieving high performance in high-frequency mapping learning. However using sine non-linearities has been shown to cause a high sensitivity to network parameters initialization. In [26], authors proposed to replace this sine non-linearities by Gaussian ones, showing good performance in image reconstruction without complex network parameters initialization schemes. Additionally, in [12], authors showed that sine non-linearities were part of a broad class of non-linearities that permitted

MLPs to learn high-frequency content. They also showed that using non-periodic non-linearities allowed to obtain good performance in novel view synthesis problems. Finally, it has recently been shown in [47] that complex Gabor wavelets could be used as activation functions, yielding good performance in a wide range of image processing problems.

B. Model-based approach

In this paper, it is proposed to use knowledge from the physics-based propagation model presented in Eq. (4) to derive a model-based neural architecture that would overcome the spectral-bias issue. As the high-frequency spatial dependency originates from $\|\mathbf{x} - \mathbf{a}_{l,j}\|_2 / \lambda_k$ in Eq. (4), it is proposed to develop this term using a Taylor expansion. It will be shown that it allows to separate the high-frequency from the low-frequency spatial content. This approach, known as the plane wave approximation, is used to obtain the well-known steering vector model [48, Chapter 7], [49].

Lemma 1. Let $\mathbf{x}_r \in \mathbb{R}^3$ be a reference location and $\mathcal{D}_x \subset \mathbb{R}^3$ be a local validity domain such that $\forall \mathbf{x} \in \mathcal{D}_x, \|\mathbf{x} - \mathbf{x}_r\|_2 \leq \epsilon_x$. Let $\mathbf{a}_{l,r} \in \mathbb{R}^3$ be a reference antenna location and $\mathcal{D}_a \subset \mathbb{R}^3$ be local validity domain such that $\forall \mathbf{a}_{l,j} \in \mathcal{D}_a, \|\mathbf{a}_{l,j} - \mathbf{a}_{l,r}\|_2 \leq \epsilon_a$. One has, $\forall (\mathbf{x}, \mathbf{a}_{l,j}) \in \mathcal{D}_x \times \mathcal{D}_a$:

$$\|\mathbf{x} - \mathbf{a}_{l,j}\|_2 \simeq \|\mathbf{x}_r - \mathbf{a}_{l,r}\|_2 + \mathbf{u}_{l,j}(\mathbf{x}_r)^\top (\mathbf{x} - \mathbf{x}_r) - \mathbf{u}_{l,r}(\mathbf{x}_r)^\top (\mathbf{a}_{l,j} - \mathbf{a}_{l,r}), \quad (6)$$

with $\mathbf{u}_{l,j}(\mathbf{x}_r) = (\mathbf{x}_r - \mathbf{a}_{l,j}) / \|\mathbf{x}_r - \mathbf{a}_{l,j}\|_2$.

Proof. See Appendix A. \square

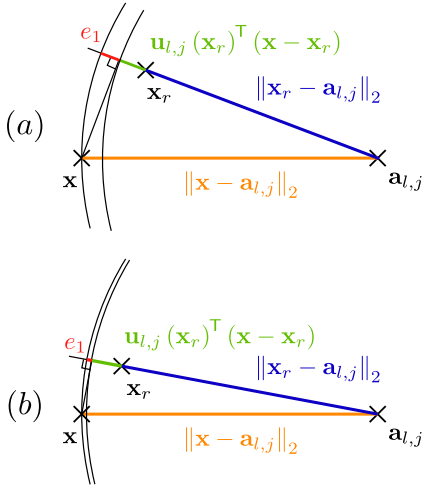


Fig. 1. Taylor expansion on locations only: (a) location \mathbf{x} far from reference \mathbf{x}_r , (b) location \mathbf{x} close to reference \mathbf{x}_r .

Fig. 1 illustrates the Taylor expansion on locations. One can remark the direct link between the approximation error and the distance to reference: when the considered location is far from the reference, the approximation error is high, while on the other hand, when the distance to the reference is small, the approximation error decreases. This emphasizes the local validity of Lemma 1. A similar analysis can be made for the Taylor expansion on antennas.

Corollary 1 proposes to analytically characterize the approximation error in Lemma 1.

Corollary 1. Let $\mathbf{x}_r \in \mathbb{R}^3$ and $\mathbf{a}_{l,r} \in \mathbb{R}^3$ be a reference location and a reference antenna location respectively. The approximation error in Eq. (6) can be approximated using the second order of the Taylor expansions as:

$$e \simeq \frac{1}{2} \left(\frac{\|\mathbf{x} - \mathbf{x}_r\|_2^2}{\|\mathbf{x}_r - \mathbf{a}_{l,j}\|_2} - o \left(\frac{1}{\|\mathbf{x}_r - \mathbf{a}_{l,j}\|_2^2} \right) + \frac{\|\mathbf{a}_{l,j} - \mathbf{a}_{l,r}\|_2^2}{\|\mathbf{x}_r - \mathbf{a}_{l,r}\|_2} - o \left(\frac{1}{\|\mathbf{x}_r - \mathbf{a}_{l,r}\|_2^2} \right) \right) \quad (7)$$

Proof. See Appendix B. \square

One can remark in Corollary 1 that the approximation error is mostly dependent on the ratios $\|\mathbf{x} - \mathbf{x}_r\|_2^2 / \|\mathbf{x}_r - \mathbf{a}_{l,j}\|_2$ and $\|\mathbf{a}_{l,j} - \mathbf{a}_{l,r}\|_2^2 / \|\mathbf{x}_r - \mathbf{a}_{l,r}\|_2$. In other words, when the distance between the reference location and current/reference antenna is important, the approximation error decreases. Indeed, in such scenario, the common far field approximation is valid, making the planar approximation of spherical wavefronts realistic. In Eq. (6), the planar wavefront term is represented by the first line projection term: this term is null when the location $(\mathbf{x} - \mathbf{x}_r)$ is orthogonal to the direction $\mathbf{u}_{l,j}(\mathbf{x}_r)$. Once introduced in a complex exponential, it yields periodic parallel level sets in the $\mathbf{u}_{l,j}(\mathbf{x}_r)$ direction. Such phenomenon constitutes the definition of planar wavefronts. On the other hand, when the reference distances are small, the far field approximation does not hold, making the approximation error being directly dependent on the distances to the references $\|\mathbf{x} - \mathbf{x}_r\|_2$ and $\|\mathbf{a}_{l,j} - \mathbf{a}_{l,r}\|_2$.

Proposition 1 presents the injection of the approximated propagation distance in the channel model in Eq. (4). This allows to obtain an approximated channel coefficient around a reference location and a reference antenna.

Proposition 1. Let $\mathbf{x}_r \in \mathbb{R}^3$ and $\mathbf{a}_{l,r} \in \mathbb{R}^3$ be a reference location and reference antenna location. Let $d_{l,r} \triangleq \|\mathbf{x}_r - \mathbf{a}_{l,r}\|_2$, $\tau_{l,r} \triangleq d_{l,r}/c$, and $h_{l,r}(\mathbf{x}_r) \triangleq e^{-j\frac{2\pi}{\lambda_r} d_{l,r}}/d_{l,r}$. Let $f_r \in \mathbb{R}$ be a reference frequency such that $\forall f_k \in \mathbb{R}, f_k = (f_k - f_r) + f_r$. One has, $\forall (\mathbf{x}, \mathbf{a}_{l,j}) \in \mathcal{D}_x \times \mathcal{D}_a$:

$$h_{j,k}(\mathbf{x}) \simeq \sum_{l=1}^{L_p} \underbrace{\gamma_l h_{l,r}(\mathbf{x}_r)}_{\text{Reference channel}} \underbrace{e^{-j\frac{2\pi}{\lambda_r} \mathbf{u}_{l,r}(\mathbf{x}_r)^\top (\mathbf{x} - \mathbf{x}_r)}}_{\text{Location correction}} \cdot \underbrace{e^{-j2\pi(f_k - f_r)\tau_{l,r}}}_{\text{Frequency correction}} \underbrace{e^{j\frac{2\pi}{\lambda_r} \mathbf{u}_{l,r}(\mathbf{x}_r)^\top (\mathbf{a}_{l,j} - \mathbf{a}_{l,r})}}_{\text{Antenna correction}} \quad (8)$$

Proof. See Appendix C. \square

It can be seen in Eq. (8) that $h_{j,k}(\mathbf{x})$ is a sum of reference channels around a reference location at a reference frequency multiplied by location, frequency, and antenna correction

terms. Letting $w_{l,r}(\mathbf{x}_r) \triangleq \gamma_l h_{l,r}(\mathbf{x}_r) e^{j\frac{2\pi}{\lambda_r} \mathbf{u}_{l,r}(\mathbf{x}_r)^T \mathbf{x}_r} \in \mathbb{C}$, Eq. (8) can be further rearranged as, $\forall (\mathbf{x}, \mathbf{a}_{l,j}) \in \mathcal{D}_{\mathbf{x}} \times \mathcal{D}_{\mathbf{a}}$:

$$h_{j,k}(\mathbf{x}_r) \simeq \sum_{l=1}^{L_p} \underbrace{w_{l,r}(\mathbf{x}) e^{-j2\pi(f_k - f_r)\tau_{l,r}} e^{j\frac{2\pi}{\lambda_r} \mathbf{u}_{l,r}(\mathbf{x}_r)^T (\mathbf{a}_{l,j} - \mathbf{a}_{l,r})}}_{\text{Slowly varying}} \cdot \underbrace{e^{-j\frac{2\pi}{\lambda_r} \mathbf{u}_{l,r}(\mathbf{x}_r)^T \mathbf{x}}}_{\text{Fastly varying}}. \quad (9)$$

Remark. One can observe in Eq. (9) that the channel coefficient $h_{j,k}(\mathbf{x})$ can be viewed as a linear combination of planar wavefronts. The directions of said planar wavefronts are defined by the spatial frequencies $\mathbf{u}_{l,r}(\mathbf{x}_r)$. Furthermore, Eq. (9) presents a spectral separation stage: the planar wavefronts present high-frequency spatial content because of their wavelength dependency in the exponential argument, while the weights, multiplied by the location and antenna-correction terms, present low-frequency spatial content (order of the Taylor-expansions validity domain).

Proposition 2 presents the expansion of the obtained approximation to every antenna and frequency, i.e. expresses the channel matrix $\mathbf{H}(\mathbf{x})$ as a function of the location \mathbf{x} .

Proposition 2. Let $\psi_{\mathbf{a},l}(\mathbf{x}) \in \mathbb{C}^{N_a}$ be a steering vector (SV) and $\psi_{\mathbf{f},l}(\mathbf{x}) \in \mathbb{C}^{N_s}$ be a frequency response vector (FRV). Let $\psi_{\mathbf{x},l}(\mathbf{x}) \triangleq e^{-j\frac{2\pi}{\lambda_r} \mathbf{u}_{l,r}(\mathbf{x}_r)^T \mathbf{x}} \in \mathbb{C}$ be a planar wavefront. The multi-antenna multi-frequency channel can be expressed as, $\forall (\mathbf{x}, \mathbf{a}_{l,j}) \in \mathcal{D}_{\mathbf{x}} \times \mathcal{D}_{\mathbf{a}}$:

$$\mathbf{H}(\mathbf{x}) \simeq \sum_{l=1}^{L_p} w_{l,r}(\mathbf{x}) \psi_{\mathbf{x},l}(\mathbf{x}) \psi_{\mathbf{a},l}(\mathbf{x}_r) \psi_{\mathbf{f},l}(\mathbf{x}_r)^T \quad (10)$$

where

$$\psi_{\mathbf{a},l}(\mathbf{x}_r) = \begin{bmatrix} e^{j\frac{2\pi}{\lambda_r} \mathbf{u}_{l,r}(\mathbf{x}_r)^T (\mathbf{a}_{l,1} - \mathbf{a}_{l,r})} \\ \vdots \\ e^{j\frac{2\pi}{\lambda_r} \mathbf{u}_{l,r}(\mathbf{x}_r)^T (\mathbf{a}_{l,N_a} - \mathbf{a}_{l,r})} \end{bmatrix} \in \mathbb{C}^{N_a}, \quad (11)$$

and

$$\psi_{\mathbf{f},l}(\mathbf{x}_r) = \begin{bmatrix} e^{-j2\pi(f_1 - f_r)\tau_{l,r}} \\ \vdots \\ e^{-j2\pi(f_{N_s} - f_r)\tau_{l,r}} \end{bmatrix} \in \mathbb{C}^{N_s}. \quad (12)$$

Proof. Direct derivation from Eq. (9) by defining SVs and FRVs. \square

The previously obtained results can be summarized as follows:

- Eq. (6) presents the Taylor expansion of the propagation distance around a reference location and reference antenna location.
- Eq. (9) presents how the Taylor expansions introduce a spectral separation stage in the propagation channel.
- Eq. (10) presents the expansion of the previous results over every antenna and frequencies.

One can remark that the approximation proposed in Eq. (10) is only valid in local neighborhoods of the reference antenna location $\mathbf{a}_{l,r}$ and reference location \mathbf{x}_r , namely $\mathcal{D}_{\mathbf{a}}$ and $\mathcal{D}_{\mathbf{x}}$. Theorem 1 presents the expansion of the approximation

validity domain to the entire \mathbb{R}^3 space. The idea is to partition \mathbb{R}^3 into location and antenna local validity domains, and then aggregate the needed planar wavefronts, SVs, and FRVs into dictionaries for each location and antenna local validity domain pair. Additionally, proof of Theorem 1 introduces the Direction of Departure (DoD) $\tilde{\mathbf{u}}_i$ so that the SV dictionary is constructed with only the physical antenna locations $\mathbf{a}_{1,j}$.

Theorem 1. Let us consider the tiling of the location subset $\mathcal{S}_{\mathbf{x}} \subset \mathbb{R}^3$ into $\Omega_{\mathbf{x}}$ local validity domains $\mathcal{D}_{\mathbf{x}}$. A second tiling is applied for the antenna subset $\mathcal{S}_{\mathbf{a}} \subset \mathbb{R}^3$ with $\Omega_{\mathbf{a}}$ local validity domains $\mathcal{D}_{\mathbf{a}}$. Let $D \in \mathbb{N}^*$ st. $D \leq L_p \Omega_{\mathbf{x}} \Omega_{\mathbf{a}}$. Let $\tilde{\Psi}_{\mathbf{a}} \in \mathbb{C}^{N_a \times D}$ be a dictionary of SVs, defined as:

$$\tilde{\Psi}_{\mathbf{a}} = \left\{ \tilde{\psi}_{\mathbf{a},i} \right\}_{i=1}^D = \left\{ \begin{bmatrix} e^{j\frac{2\pi}{\lambda_r} \tilde{\mathbf{u}}_i^T (\mathbf{a}_{1,1} - \mathbf{a}_{1,r})} \\ \vdots \\ e^{j\frac{2\pi}{\lambda_r} \tilde{\mathbf{u}}_i^T (\mathbf{a}_{1,N_a} - \mathbf{a}_{1,r})} \end{bmatrix} \right\}_{i=1}^D, \quad (13)$$

where $\tilde{\mathbf{u}}_i \in \mathbb{R}^3$ is a DoD. Let $\tilde{\Psi}_{\mathbf{f}} \in \mathbb{C}^{N_s \times D}$ be a dictionary of FRVs, defined as:

$$\tilde{\Psi}_{\mathbf{f}} = \left\{ \tilde{\psi}_{\mathbf{f},i} \right\}_{i=1}^D = \left\{ \begin{bmatrix} e^{-j2\pi(f_1 - f_r)\tau_i} \\ \vdots \\ e^{-j2\pi(f_{N_s} - f_r)\tau_i} \end{bmatrix} \right\}_{i=1}^D, \quad (14)$$

where $\tau_i \in \mathbb{R}^+$ is a propagation delay. Let $\tilde{\psi}_{\mathbf{x}}(\mathbf{x}) \in \mathbb{C}^D$ be a dictionary of planar wavefronts, defined as:

$$\tilde{\psi}_{\mathbf{x}}(\mathbf{x}) = \left\{ \tilde{\psi}_{\mathbf{x},i} \right\}_{i=1}^D = \left\{ e^{-j\frac{2\pi}{\lambda_r} \mathbf{u}_i^T \mathbf{x}} \right\}_{i=1}^D, \quad (15)$$

where $\mathbf{u}_i \in \mathbb{R}^3$ a spatial frequency. Finally, let $\mathbf{w}(\mathbf{x}) \in \mathbb{C}^D$ be an activation vector such that: $\varpi(\mathbf{x}) = \mathbf{w}(\mathbf{x}) \odot \tilde{\psi}_{\mathbf{x}}(\mathbf{x})$. Then, $\forall \mathbf{x} \in \mathbb{R}^3$:

$$\mathbf{H}(\mathbf{x}) \simeq \sum_{i=1}^D \varpi_i(\mathbf{x}) \tilde{\psi}_{\mathbf{a},i} \tilde{\psi}_{\mathbf{f},i}^T \quad (16)$$

with $\|\varpi(\mathbf{x})\|_0 = L_p$,

Proof. See Appendix D. \square

One can see that Theorem 1 proposes a sparse continuous interpolation of the channel matrix. The composite dictionary consists of all possible combinations of the required SVs and FRVs, while the activation vector presents spectral separation: it is defined with a low-frequency term $\mathbf{w}(\mathbf{x})$, and a high-frequency term $\tilde{\psi}_{\mathbf{x}}(\mathbf{x})$.

Remark. While Theorem 1 extends the validity expansion of Eq. (10) to the entire \mathbb{R}^3 space, the number of atoms D in each dictionary is intractable due to its dependence on the number of local validity domains $\Omega_{\mathbf{x}}$ and $\Omega_{\mathbf{a}}$. A way to overcome this issue is to construct each dictionary by discretizing its generating subspace, i.e. the DoD subspace, unit sphere \mathcal{S}_1 , for the SV dictionary, the delay subspace \mathbb{R}^+ for the FRV dictionary and the spatial frequency subspace \mathcal{S}_1 for the planar wavefront dictionary. This approach is at the center of the model-based neural network architecture presented in Section IV.

C. Discussion: a sparse recovery approach

As Eq. (16) can be viewed as a sparse reconstruction problem, one could think of finding the correct activation coefficients using sparse recovery techniques. Indeed, using matching pursuit (MP)/orthogonal matching pursuit (OMP) algorithms [50], [51], one could find a sparse representation of $\mathbf{H}(\mathbf{x})$ in a composite dictionary of FRVs/SVs. Obtaining a channel estimate $\hat{\mathbf{H}}(\mathbf{x})$ at a wanted location \mathbf{x} could be separated into two stages. Firstly, one would have to solve:

$$\begin{aligned} \min_{\mathbf{w}} \quad & \left\| \mathbf{H}(\mathbf{x}_r) - \sum_{i=1}^D w_i \tilde{\psi}_{\mathbf{x},i}(\mathbf{x}_r) \tilde{\psi}_{\mathbf{a},i} \tilde{\psi}_{\mathbf{f},i}^T \right\|_F^2, \\ \text{s.t.} \quad & \|\mathbf{w}\|_0 = L_p, \end{aligned} \quad (17)$$

$\forall \mathbf{x}_r \in \mathcal{H}_r \subset \mathbb{R}^3$, \mathcal{H}_r being a set of reference locations. Then, for the wanted location \mathbf{x} , one could obtain the channel estimate as:

$$\hat{\mathbf{H}}(\mathbf{x}) = \sum_{i=1}^D w_{\mathbf{x}_r^*,i} \tilde{\psi}_{\mathbf{x},i}(\mathbf{x}) \tilde{\psi}_{\mathbf{a},i} \tilde{\psi}_{\mathbf{f},i}^T, \quad (18)$$

where $w_{\mathbf{x}_r^*} \in \mathbb{C}$ is the activation coefficient obtained by solving Eq. (17) for $\mathbf{x}_r^* = \arg \min_{\mathbf{x}_r \in \mathcal{H}_r} \|\mathbf{x} - \mathbf{x}_r\|_2$, i.e. the closest reference location to the wanted location.

However this approach presents an intractable complexity induced by the high-frequency nature of the propagation channel and the composite dictionary size. Indeed, as the propagation channel is a function rapidly varying with the location, one would have to consider spatially close reference locations, i.e. with spacing between reference locations under the wavelength. This introduces a high cardinality in \mathcal{H}_r , which increases the time complexity for achieving the first step of this estimation scheme. Additionally, as the composite dictionary is composed of every pair of FRVs/SVs, it results in a prohibitive dictionary size, further increasing the time complexity of the first estimation step.

The next section proposes to transform the obtained channel approximation in Eq. (16) into a neural architecture, following the model-based machine learning paradigm.

IV. MODEL-BASED NEURAL ARCHITECTURE

As it has been shown that classical signal processing methods are unsuited for solving the sparse reconstruction problem in Theorem 1, it is proposed to leverage the learning capabilities of neural networks for the location-to-channel mapping learning. This section presents a model-based neural architecture from Eq. (16).

The approximation in Eq. (16) can be rewritten using the vectorization operator, clearly displaying the sparse representation structure of the approximated channel. $\forall \mathbf{x} \in \mathbb{R}^3$:

$$\text{vec}(\mathbf{H}(\mathbf{x})) \simeq (\tilde{\Psi}_{\mathbf{f}}(\mathbf{x}) \otimes \tilde{\Psi}_{\mathbf{a}}(\mathbf{x})) \text{vec}(\text{diag}(\boldsymbol{\varpi}(\mathbf{x}))) \quad (19)$$

with $\|\boldsymbol{\varpi}(\mathbf{x})\|_0 = L_p$,

As shown in Eq. (19), the location-to-channel mapping learning problem can be partitioned into four subproblems: the planar wavefronts, FRV, SV dictionaries, and the complex weights coefficients learning.

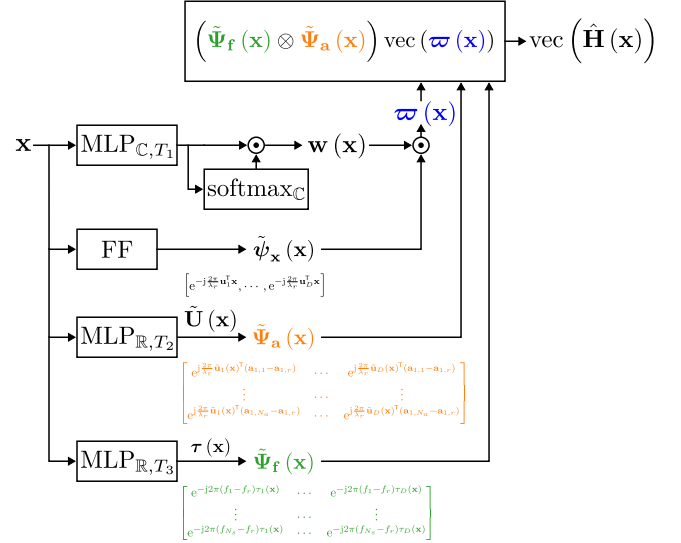


Fig. 2. Proposed model-based neural architecture.

A. Planar wavefront dictionary

As exposed by the previous analysis, the planar wavefronts take the form $\tilde{\psi}_{\mathbf{x}}(\mathbf{x}) = \{e^{-j\frac{2\pi}{\lambda_r} \mathbf{u}_i^T \mathbf{x}}\}_{i=1}^D \in \mathbb{C}^D$. Such dictionary can be constructed from the spatial frequencies $\mathbf{u}_i \in \mathbb{R}^3$, which by definition, are unit vectors representing the planar wavefronts direction. As a result, every spatial frequency belongs to a two-dimensional manifold: the unit sphere \mathcal{S}_1 . Sampling \mathcal{S}_1 with D points yields the spatial frequency dictionary $\mathbf{U} \triangleq \{\mathbf{u}_i\}_{i=1}^D \in \mathbb{R}^{3 \times D}$ that is used to compute the planar wavefront dictionary. The dictionary $\tilde{\psi}_{\mathbf{x}}(\mathbf{x})$ is then constructed using the Fourier feature (FF) layer, defined as:

$$\text{FF} : \mathbf{x} \rightarrow [e^{-j\frac{2\pi}{\lambda_r} \mathbf{u}_1^T \mathbf{x}}, \dots, e^{-j\frac{2\pi}{\lambda_r} \mathbf{u}_D^T \mathbf{x}}]. \quad (20)$$

Note that this FF layer is just a complex implementation of the cos/sin embedding layer used in RFF networks [23], [24]. Also note that spatial frequencies could be learned either by gradient descent or directly through a neural network, however, they are kept fixed for this study.

B. FRV dictionary

It has been presented in Eq. (14) that the FRV dictionary $\tilde{\Psi}_{\mathbf{f}}(\mathbf{x}) \in \mathbb{C}^{N_s \times D}$ only depends on the system frequencies f_k , the reference frequency f_r , and propagation delays τ_i . The system and reference frequencies are assumed to be known: such assumption is typically made in classical communication systems. In this study, the reference frequency is computed as $f_r = \frac{1}{N_s} \sum_{k=1}^{N_s} f_k$. The FRV dictionary can then be constructed by sampling the propagation delay subspace, i.e. \mathbb{R}^+ . In order to optimize the performance of the proposed approach, it is suggested to learn the discretization for every location. As such, it is proposed to use a MLP that learns a propagation delay vector $\boldsymbol{\tau}(\mathbf{x}) \in \mathbb{R}^D$ for every location \mathbf{x} . Indeed, as the propagation delay vector exhibits slow variations in the location space, the MLP will not suffer from the spectral bias.

C. SV dictionary

As presented in Eq. (13), the SV dictionary $\tilde{\Psi}_{\mathbf{a}}(\mathbf{x}) \in \mathbb{C}^{N_a \times D}$ only depends on the reference frequency wavelength λ_r , on the true antenna locations $\mathbf{a}_{1,j}$, on the true reference antenna location $\mathbf{a}_{1,r}$, and on DoDs $\tilde{\mathbf{u}}_i$. The reference frequency wavelength is assumed to be known, as well as the antenna locations. The true reference antenna location is computed as the barycenter of the true antenna locations. In order to construct the SV dictionary, one could discretize the DoD subspace \mathcal{S}_1 . Similarly than for the FRV dictionary, it is proposed to optimize performance by learning the discretization for every location. As such, it is proposed to learn $\tilde{\mathbf{U}}(\mathbf{x})$ using a MLP, a method referred to as MB- $\tilde{\mathbf{u}}$ learning. On the other hand, it is proposed to directly learn the entire SV dictionary for each location using a MLP, without assuming any dictionary structure. This approach, referred to as MB- $\tilde{\Psi}_{\mathbf{a}}$ learning releases constraints on the antenna correction terms at the expense of an increased learning-parameter complexity.

D. Complex weights learning

The complex activation weights $\mathbf{w}(\mathbf{x}) \in \mathbb{C}^D$ are learned following the same approach as in [42]. A MLP is used to learn the complex weight vector, $\mathbf{w}(\mathbf{x}) \in \mathbb{C}^D$, introducing the sparsity constraint with a softmax ponderation.

E. Global architecture

The proposed model-based neural network architecture for the location-to-channel mapping learning is presented in Fig. 2. Note that this architecture only presents the MB- $\tilde{\mathbf{u}}$ approach. During experiments, the used approach will be explicitly specified. Also note that $\text{MLP}_{\mathbb{C},T}$ represents a 3-layer $\text{ReLU}_{\mathbb{C}}$ -MLP¹ with complex weights and biases, where each layer width is T . $\text{MLP}_{\mathbb{R},T}$ represents the same MLP but with real weights/biases and ReLU activation functions.

The following remark emphasizes that the use of hypernetworks is a key feature of the proposed model.

Remark. *The proposed architecture shares common features with classical INR networks. Indeed, the FF layer can be seen as a positional-embedding stage, where the low dimensional location information is projected on a higher dimensional space containing high spatial frequencies. Nevertheless, the proposed architecture stands out from classical INR networks with the introduction of hypernetworks [52], [53], i.e. parallel neural networks learning parameters of the main network. Four hypernetworks are used in Fig. 2, in order to constitute the complex activation vector and the planar wavefront/SV/FRV dictionaries.*

V. EXPERIMENTS

In this section, the mapping-learning performance of the proposed approach are evaluated on realistic synthetic data. Additionally, its performance is compared against classical architecture from the INR literature.

¹Note that $\forall z_1 \in \mathbb{C}, \forall z_2 \in \mathbb{C}^N, \text{ReLU}_{\mathbb{C}}(z_1) = \text{ReLU}(\Re\{z_1\}) + j\text{ReLU}(\Im\{z_1\})$ and $\text{softmax}_{\mathbb{C}}(z_2) = \text{softmax}(|z_2|)$.

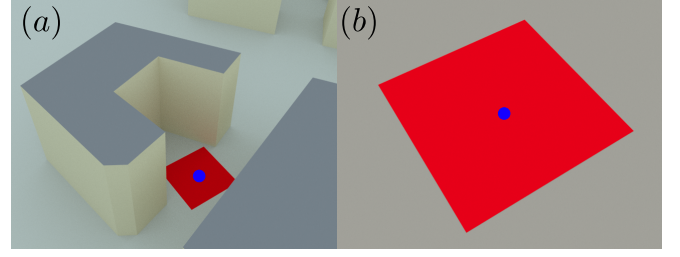


Fig. 3. Ray-tracing scenes in Sionna: the red plane represents the possible train/test locations and the blue dot represents the BS. (a): scene used for \mathcal{D}_1 and \mathcal{D}_2 . (b): scene used for \mathcal{D}_3 .

A. Learning framework

The dataset generation can be divided into two phases: location generation and channel computation at those locations.

System parameters. For all datasets, the central frequency (i.e. the reference frequency f_r) is set to 3.5GHz and the considered bandwidth is 50MHz. The BS is equipped with a uniform linear array (ULA) with half reference wavelength spacing. The number of considered antennas N_a and frequencies N_s is presented for each experiment.

Location generation. For all datasets, a 10m by 10m square scene is considered as the location space. Inside this scene, train locations are uniformly sampled with a certain location density. Test locations consists of a uniform grid with $\lambda/4$ sampling in both directions. In the considered scene and at the considered reference frequency, this grid yields around 210k locations, enabling a thorough assessment of the mapping learning capabilities. Additionally, the spatial proximity of test locations allows to assess the learning performance of small scale channel fading.

Remark. *Note that while all previous theoretical developments are proven in the \mathbb{R}^3 scenario, the following simulations of the location-to-channel mapping learning are obtained in \mathbb{R}^2 due to computational complexity. Hence, for all datasets, the locations are considered on the same elevation plane as the BS, i.e. considering 2D locations and azimuth DoDs. Consequently, spatial frequencies are sampled from the \mathcal{C}_1 unit circle.*

Channel generation. Realistic synthetic channels are generated using the Sionna ray-tracing library [54]. For each train/test location, ray-tracing techniques find the propagation paths and compute the channel coefficients. Four different datasets are considered:

- \mathcal{D}_1 : complex dataset with variable number of propagation paths regarding the considered location in the scene.
- \mathcal{D}_2 : \mathcal{D}_1 with no LoS path.
- \mathcal{D}_3 : LoS dataset.

As depicted in Fig. 3, \mathcal{D}_1 and \mathcal{D}_2 are generated in the *Etoile* Sionna scene in Paris, while \mathcal{D}_3 is generated in an empty scene. For all datasets, diffraction and scattering are not considered. In \mathcal{D}_1 and \mathcal{D}_2 , each propagation path can present at most two consecutive reflections.

Training loss and evaluation metric. All networks are

trained using the classical ℓ_F loss, defined as:

$$\mathcal{L} = \frac{1}{|\mathcal{B}|} \sum_{\mathbf{x} \in \mathcal{B}} \|\mathbf{H}(\mathbf{x}) - f_{\theta}(\mathbf{x})\|_F^2, \quad (21)$$

where $f_{\theta}(\mathbf{x}) = \hat{\mathbf{H}}(\mathbf{x})$ is the output of the neural network, and $\mathcal{B} \subset \mathbb{R}^2$ is the current batch set for the considered scene. The evaluation metric is the Normalized Mean Squared Error (NMSE) in dB over the test grid, defined as:

$$\text{NMSE}_{(\text{dB})} = 10 \log_{10} \left(\frac{1}{|\mathcal{T}|} \sum_{\mathbf{x} \in \mathcal{T}} \frac{\|\mathbf{H}(\mathbf{x}) - f_{\theta}(\mathbf{x})\|_F^2}{\|\mathbf{H}(\mathbf{x})\|_F^2} \right), \quad (22)$$

where $\mathcal{T} \subset \mathbb{R}^2$ is the test location set for the considered scene.

B. Baselines

It is proposed to assess the performance of the proposed architecture against baseline models from the INR literature. As such, several baselines are proposed in Fig.4: 1. is a classical complex MLP while 2. and 3. are complex RFFs. Additionally, in 2., the spatial frequencies are drawn from a gaussian distribution, while 3. considers the same spatial frequencies as in the model-based architecture, i.e. sampled from the \mathcal{C}_1 circle. All MLPs output a vector of dimension $N_a N_s$ which is then reshaped to obtain the estimated channel matrix $\hat{\mathbf{H}}(\mathbf{x}) \in \mathbb{C}^{N_a \times N_s}$.

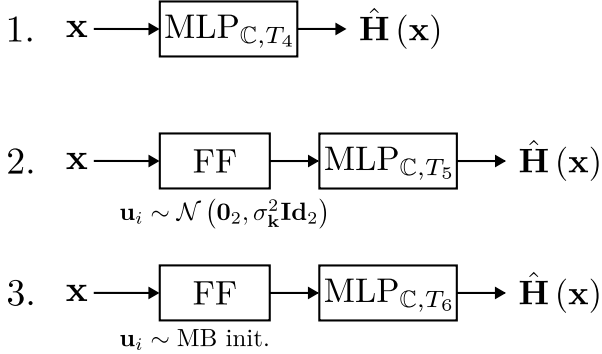


Fig. 4. Baselines: 1. MLP, 2. and 3. RFFs.

C. Experimental results

For all experiments, the proposed networks and baselines have the following layer sizes: $T_1 = 256$, $T_2 = T_3 = 64$, $T_4 = 1024$, and $T_5 = T_6 = 64$. Additionally, unless stated otherwise, $D = 1000$ spatial frequencies are considered. Those values have been empirically chosen to maximize performance and minimize overfitting. For RFFs, increasing the number of learning parameters did not improve performance. Finally, a training location density of $175 \text{locs./m}^2 \simeq 1.3 \text{locs./}\lambda^2$ is considered at the exception of the experiment depicted in Fig. 6. **Scene reconstruction.** Let $N_a = 64$, $N_s = 64$. It is proposed to study the ability of each network to learn the location-to-channel mapping in different radio-environments.

Table I presents the reconstruction results. One can remark that the proposed MB- $\tilde{\Psi}_a$ model outperforms every baseline and the other MB model in every propagation scene.

TABLE I
NMSE_(dB) OVER THE TEST GRID.

	MLP	RFF	RFF (MB init.)	MB- $\tilde{\Psi}_a$	MB- $\tilde{\mathbf{u}}$
Params.	10.5M	669k	669k	9.1M	851k
\mathcal{D}_1	0.01	0.02	2.10^{-3}	-29.23	-14.60
\mathcal{D}_2	0.01	0.05	3.10^{-3}	-20.19	-10.25
\mathcal{D}_3	0.01	0.02	2.10^{-3}	-40.67	-11.40

The performance gap observed between the MB- $\tilde{\Psi}_a$ and MB- $\tilde{\mathbf{u}}$ models is due to an hypothesis made in the proof of Proposition 1 and is explained in a subsequent experiment. The bad mapping learning capabilities of the baselines can be explained by the lack of structure of their architecture.

Fig. 5 presents the reconstructed channel after training for several models. It clearly appears that the MB network efficiently learns the desired mapping. Additionally, one can remark that the RFF model presents high-frequency spatial contents due to its embedding stage, but fails to learn the complex structure of the propagation channel. Finally, the reconstructed channel for the MLP model presents low-frequency spatial contents, illustrating the spectral-bias issue for this architecture.

Fig. 6 presents the mapping-learning performance evolution with respect to the training location density on the \mathcal{D}_1 dataset. One can remark that the MB- $\tilde{\Psi}_a$ network outperforms the baseline in any density configuration. Additionally, the proposed network presents a failure mode in the low location density regime. In this regime, the scarcity of spatially close training locations results in the learning failure of the rapidly varying spatial content. Note that the proposed method achieves quasi perfect reconstruction in sub-Shannon-Nyquist location density, as the 2D Shannon-Nyquist criterion yields a density of $4 \text{locs./}\lambda^2$.

Fig. 7 presents the ground-truth and estimated frequency/antenna responses for a given test location in the \mathcal{D}_1 dataset. One can see that, due to the multipath nature of the \mathcal{D}_1 scene, the frequency response presents rapid variations. Both the estimated frequency and antenna responses are close to the ground-truth highlighting the very good reconstruction performance of the proposed model network.

Generalization capabilities. Fig. 8 presents the frequency generalization performance of the MB- $\tilde{\Psi}_a$ model trained on the \mathcal{D}_1 dataset with $N_s = 32$, and evaluated on $N_s = 64$ frequencies. The dashed line in Fig. 8 represents the train/test frequency separation. The NMSE, computed over the test locations, for each frequency at the central antenna, is unsurprisingly higher for the frequency unseen during frequency but still remains low. It highlights the generalization capabilities of the model-based network: as the FRV hypernetwork learns propagation delays, it successfully learns the physics of the propagation scene and is agnostic to the considered frequencies. This is illustrated on the right side of Fig. 8, where the reconstructed channel for a given location \mathbf{x}_1 is almost perfect on the frequencies used during training, and still follows the ground-truth for frequencies not seen during training.

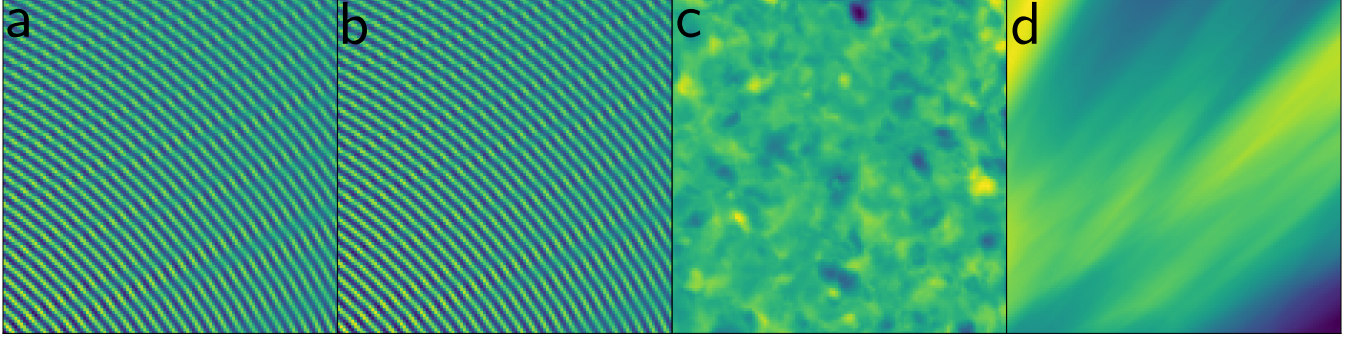


Fig. 5. Real part of reconstructed channel over a 2.5m by 2.5m of \mathcal{D}_1 , for the central antenna and frequency ($N_a = 64$, $N_s = 64$), a: Ground Truth, b: MB- $\tilde{\Psi}_a$, c: RFF, d: MLP.

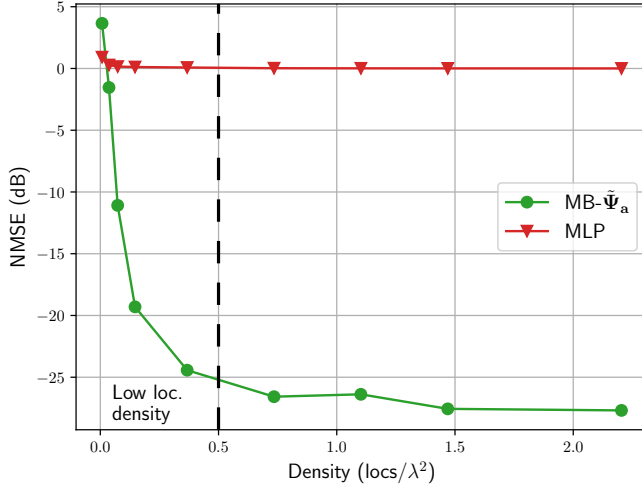


Fig. 6. NMSE evolution with the training location density: MB- $\tilde{\Psi}_a$ learning, \mathcal{D}_1 dataset ($N_a = 64$, $N_s = 64$).

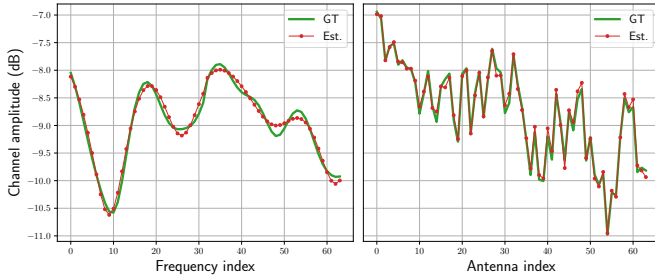


Fig. 7. Reconstruction performance for a given location \mathbf{x}_0 : MB- $\tilde{\Psi}_a$ learning, \mathcal{D}_1 dataset ($N_a = 64$, $N_s = 64$).

Radio-environment compression. Let $N_a = 64$, $N_s = 64$. Let us consider the transmission (or storage) of the test dataset: in addition to the location information, one has to transmit $2N_a N_s N_l$ real numbers where N_l is the number of locations. As the test location grid is very dense ($N_l \simeq 210k$), it could be more efficient to only transmit the weights of the trained model-based architecture. Indeed, as the MB- $\tilde{\Psi}_a$ model achieves good location-to-channel mapping learning, one can use this network and the transmitted locations to reconstruct the channel. As an example, when considering encoding of variables on 32bits, the channel coefficients

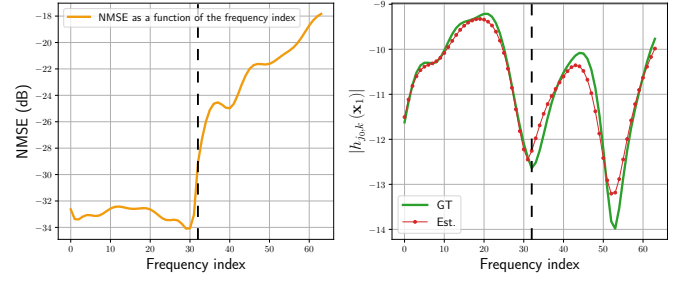


Fig. 8. Frequency generalization performance: MB- $\tilde{\Psi}_a$ learning, \mathcal{D}_1 dataset ($N_a = 64$, $N_s = 32$ for training, $N_s = 64$ for testing).

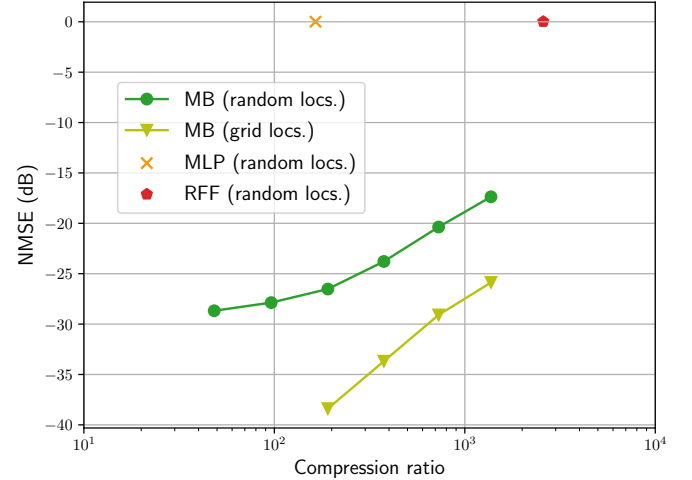


Fig. 9. Learning performance evolution with the compression ratio: MB- $\tilde{\Psi}_a$ learning, \mathcal{D}_1 dataset ($N_a = 64$, $N_s = 64$).

over the test grid weight around 6.9Go while the 9.1M learning parameters of the MB- $\tilde{\Psi}_a$ model (with $D = 1000$) only weight around 36.4Mo. Let N_b be the number of real learnable coefficients of the proposed neural architecture, the compression ratio is then defined as $R = 2N_a N_s N_l / N_b$.

Fig. 9 presents the evolution of the learning performance with respect to the compression ratio R for various networks. It can be shown that the number of sampled spatial frequencies D is predominant on the learning error for the MB models. Therefore, it is proposed to only vary this parameter to vary N_b . The random locs. approach refers to the training on

random locations with $1.3\text{locs.}/\lambda^2$ spatial density, while the grid locs. refers to the training on the entire $\lambda/4$ uniform grid. One can remark in Fig. 9 that, even at high compression ratios, the NMSE of the MB- $\tilde{\Psi}_a$ model remains significantly low, highlighting the efficiency of the proposed approach for radio-environment compression. One can also note that, when considering the grid locs. approach, the model-based network reaches very good reconstruction performance, with a NMSE performance increase by around 10dB in comparison to the random locs. approach. Therefore, it enables the transmission of the dataset through the network weights with minimal reconstruction error, at the expense of a longer training phase. Finally, one should note that the compression ratio is virtually infinite. Indeed, as the trained network efficiently learns the location-to-channel mapping, it is able to infer the channel matrix for any location in the considered scene with good performance.

Performance evolution with N_a and N_s . Fig. 10 exposes the performance evolution along the antenna array and system frequencies for the MB- \tilde{u} learning network, trained on the D_1 dataset with $N_a = 64$, $N_s = 64$. It presents the NMSE along the antenna indexes, computed over the test grid at the central frequency, and the NMSE along the frequency indexes, computed over the test grid at the central antenna. One can observe that, while the NMSE is almost constant over the different frequencies, it rises on the antenna array sides. This can be explained through the previous theoretical developments: the model-based network has been designed with two Taylor expansions, one on the locations and another on the antennas. When the considered antenna array is large, the antenna correction terms fail for the array sides due the local nature of the Taylor expansion. This results in an increased error response on the antenna array sides. On the other hand, as the frequency correction terms do not originate from an approximation (see Eq. (27) in Appendix A), the error response over the different system frequencies does not exhibit error spikes. It motivates the use of the MB- $\tilde{\Psi}_a$ model which drops the model-based constraints for the FRV dictionary, overcoming this side effect. Note that a more extensive comparison between the two architectures is presented in the following experiment.

Fig. 11 presents the performance evolution with respect to the number of frequencies by setting $N_a = 2$ and letting N_s vary over the fixed 50MHz bandwidth, for the MB- $\tilde{\Psi}_a$ model. One can remark that the NMSE curve presents a minor performance degradation when N_s increases from 1 to 8 and then remains constant for higher values of N_s . As the FRV hypernetwork is independent on the number of frequencies, increasing the number of frequencies is equivalent to considering a harder learning problem with the same number of learning parameters. This explains the minor performance degradation when N_s increases. However note that, even with $N_s = 64$, the NMSE performance remains satisfactory. Additionally, the adaptability of the proposed architecture is enhanced: in [42], the proposed network was only able to learn the location-to-channel mapping for a unique antenna and frequency. Directly transposing the model-based architecture of [42] for multi-antenna/multi-frequency would require one parallel model for each wanted antenna/frequency

pair. In this paper, the proposed model-based architecture directly scales with the number of frequencies: as the FRV hypernetwork is independent on N_s , one can use the same network for any wanted N_s with the same learning-parameter complexity. The only complexity difference comes from Kronecker product of Eq. (19), which is negligible compared to the total numbers of operations in the neural network.

MB- $\tilde{\Psi}_a$ learning vs MB- \tilde{u} learning. During the theoretical developments of Proposition 1, the hypothesis of DoD equality over the entire antenna array has been made to obtain Eq. (8). This hypothesis fails in two scenarios, presented in Fig. 12: when the considered scene is close to the antenna array, and when the considered scene is far from a large antenna array.

Fig. 13 presents the performance evolution with respect to the number of antennas for $N_s = 2$ and both the MB- $\tilde{\Psi}_a$ and MB- \tilde{u} models trained on the D_3 dataset. One can remark that the NMSE increases with the number of antennas for the MB- \tilde{u} model: this is an immediate consequence of the aforementioned failure scenarios. As the propagation scene for the D_3 dataset consists of a small zone around the BS, when one increases the number of antennas, the DoD equality across antennas does not hold anymore, resulting in a performance loss. This phenomenon is absent for the MB- $\tilde{\Psi}_a$ model: in this architecture, the entire FRV matrix is learned, overcoming the DoD assumption issue.

VI. CONCLUSION AND FUTURE WORK

This paper presented a study on the location-to-channel mapping learning problem. Through analytical developments based on Taylor expansions of the propagation distance, a model-based neural architecture was proposed. Its performance have been studied on realistic channels against several baselines from the Implicit Neural Representation literature, showing great mapping learning performance in several realistic propagation scenes. It also showed that the proposed architecture overcame the spectral bias issue. Additionally, the use of the proposed network for radio-environment compression has been exposed. Transmitting the parameters of the trained model-based model and reconstructing the channel coefficients at different locations has been proven to be more efficient than directly transmitting the channel coefficients, with compression ratio reaching 10^3 without major performance loss. Finally, the theoretical developments made to obtain the approximated channel model have been leveraged to explain the model-based architecture performance in several scenarios, demonstrating the great interpretability of the model-based machine learning paradigm.

Future work will consider the optimization of the proposed architecture learning-parameter number. This could be done by reducing the number of planar wavefronts and optimizing them through an update rule or gradient descent. Future work could also consider the proposed method in a time-varying scene, i.e. with mobility. It may be possible to train the scene from channel samples in the static scenario and then use an online learning strategy to continuously adapt the learned mapping with channel samples taking into account mobility.

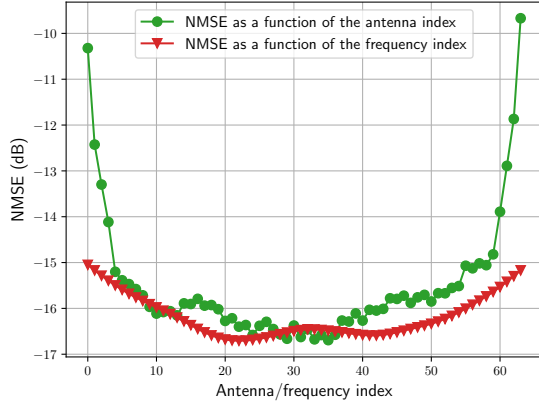


Fig. 10. NMSE evolution with antenna/frequency index: MB- $\tilde{\mathbf{u}}$ learning, \mathcal{D}_1 dataset ($N_a = 64$, $N_s = 64$).

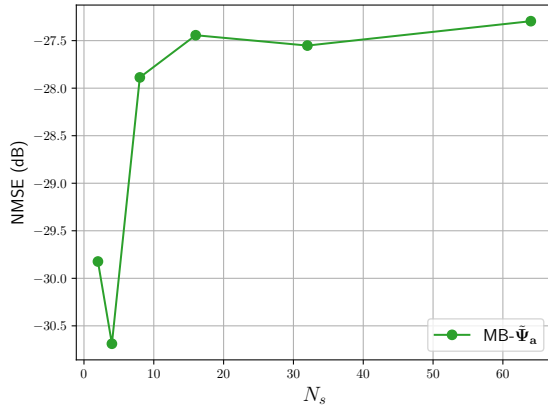


Fig. 11. NMSE evolution with N_s : MB- $\tilde{\Psi}_a$ learning, \mathcal{D}_1 dataset ($N_a = 2$).

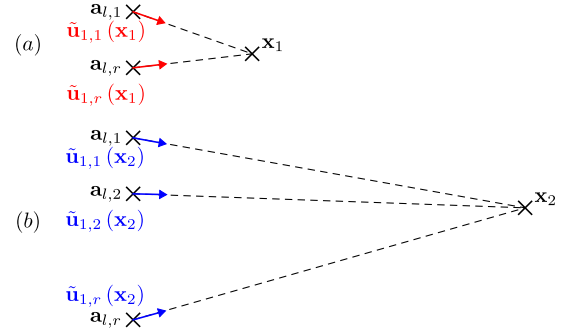


Fig. 12. Failure scenarios for the DoD equality hypothesis: (a) locations close to the antenna array, (b): locations far from a large antenna array.

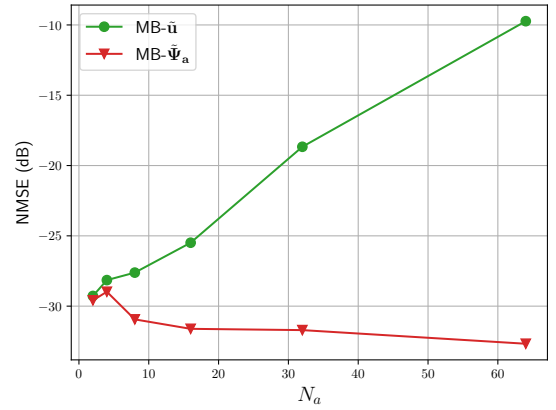


Fig. 13. NMSE evolution with N_a : \mathcal{D}_3 dataset ($N_s = 2$).

REFERENCES

- [1] N. Shlezinger, J. Whang, Y. C. Eldar, and A. G. Dimakis, "Model-based deep learning," *Proc. of the IEEE*, vol. 111, no. 5, pp. 465–499, 2023.
- [2] H. He, C.-K. Wen, S. Jin, and G. Y. Li, "Deep learning-based channel estimation for beamspace mmwave massive MIMO systems," *IEEE Wireless Commun. Lett.*, vol. 7, no. 5, pp. 852–855, 2018.
- [3] X. Wei, C. Hu, and L. Dai, "Deep learning for beamspace channel estimation in millimeter-wave massive MIMO systems," *IEEE Trans. on Commun.*, vol. 69, no. 1, pp. 182–193, 2021.
- [4] T. Yassine and L. Le Magoarou, "mpNet: Variable depth unfolded neural network for massive MIMO channel estimation," *IEEE Trans. on Wireless Commun.*, vol. 21, no. 7, pp. 5703–5714, 2022.
- [5] B. Chatelier, L. Le Magoarou, and G. Redieteb, "Efficient deep unfolding for SISO-OFDM channel estimation," in *IEEE Int. Conf. on Commun. (ICC)*, 2023.
- [6] D. H. Shmuel, J. P. Merkofer, G. Revach, R. J. G. van Sloun, and N. Shlezinger, "Subspacenet: Deep learning-aided subspace methods for doa estimation," 2023.
- [7] T. Yassine, L. L. Magoarou, S. Paquelet, and M. Crussière, "Leveraging triplet loss and nonlinear dimensionality reduction for on-the-fly channel charting," in *2022 IEEE 23rd Int. Workshop on Signal Proc. Advances in Wireless Commun.*, 2022, pp. 1–5.
- [8] T. Yassine, B. , V. Corlay, M. Crussière, S. Paquelet, O. Tirkkonen, and L. L. Magoarou, "Model-based deep learning for beam prediction based on a channel chart," in *2023 57th Asilomar Conf. on Signals, Syst., and Comput.*, 2023, pp. 1636–1640.
- [9] T. Yassine, L. L. Magoarou, M. Crussière, and S. Paquelet, "Optimizing multicarrier multiantenna systems for los channel charting," *arXiv preprint*, 2023.
- [10] J. M. Mateos-Ramos, B. Chatelier, C. Häger, M. F. Keskin, L. L. Magoarou, and H. Wymeersch, "Semi-supervised end-to-end learning for integrated sensing and communications," 2023.
- [11] B. Mildenhall, P. P. Srinivasan, M. Tancik, J. T. Barron, R. Ramamoorthi, and R. Ng, "Nerf: Representing scenes as neural radiance fields for view synthesis," *Commun. ACM*, vol. 65, no. 1, p. 99–106, 2021.
- [12] S. Ramasinghe and S. Lucey, "Beyond periodicity: Towards a unifying framework for activations in coordinate-mlps," in *Proc. of the Eur. Conf. on Comput. Vis.*, 2022, pp. 142–158.
- [13] J. Zheng, S. Ramasinghe, and S. Lucey, "Rethinking positional encoding," *ArXiv*, Jul. 2021.
- [14] G. Yuce, G. Ortiz-Jimenez, B. Besbinar, and P. Frossard, "A structured dictionary perspective on implicit neural representations," in *IEEE/CVF Comput. Soc. Conf. Comput. Vis. Pattern Recognit.*, Jun. 2022.
- [15] S. Ramasinghe, L. E. MacDonald, and S. Lucey, "On the frequency-bias of coordinate-mlps," in *Advances in Neural Inf. Process. Syst.*, vol. 35, 2022, pp. 796–809.
- [16] H. Saratchandran, S.-F. Chng, and S. Lucey, "Analyzing the neural tangent kernel of periodically activated coordinate networks," *arXiv preprint*, Feb. 2024.
- [17] H. Saratchandran, S. Ramasinghe, V. Shevchenko, A. Long, and S. Lucey, "A sampling theory perspective on activations for implicit neural representations," *arXiv preprint*, Feb. 2024.
- [18] G. Cybenko, "Approximation by superpositions of a sigmoidal function," *Mathematics of control, signals and systems*, vol. 2, no. 4, pp. 303–314, 1989.
- [19] K. Hornik, M. Stinchcombe, and H. White, "Multilayer feedforward networks are universal approximators," *Neural networks*, vol. 2, no. 5, pp. 359–366, 1989.
- [20] N. Rahaman, A. Baratin, D. Arpit, F. Draxler, M. Lin, F. Hamprecht, Y. Bengio, and A. Courville, "On the spectral bias of neural networks," in *Int. Conf. on Mach. Learn.*, 2019, pp. 5301–5310.
- [21] Y. Cao, Z. Fang, Y. Wu, D.-X. Zhou, and Q. Gu, "Towards understanding the spectral bias of deep learning," in *Proc. of the Thirtieth Int. Joint Conf. on Artif. Intell., IJCAI-21*, 2021, pp. 2205–2211.

- [22] Z.-Q. John Xu, Y. Zhang, T. Luo, Y. Xiao, and Z. Ma, “Frequency principle: Fourier analysis sheds light on deep neural networks,” *Commun. in Comput. Phys.*, vol. 28, no. 5, pp. 1746–1767, 2020.
- [23] A. Rahimi and B. Recht, “Random features for large-scale kernel machines,” in *Adv. Neural Inf. Process.*, vol. 20, 2007.
- [24] M. Tancik, P. Srinivasan, B. Mildenhall, S. Fridovich-Keil, N. Raghavan, U. Singhal, R. Ramamoorthi, J. Barron, and R. Ng, “Fourier features let networks learn high frequency functions in low dimensional domains,” *Advances in Neural Inf. Process. Syst.*, vol. 33, pp. 7537–7547, 2020.
- [25] V. Sitzmann, J. Martel, A. Bergman, D. Lindell, and G. Wetzstein, “Implicit neural representations with periodic activation functions,” *Advances in Neural Inf. Process. Syst.*, vol. 33, pp. 7462–7473, 2020.
- [26] S.-F. Chng, S. Ramasinghe, J. Sherrah, and S. Lucey, “Gaussian activated neural radiance fields for high fidelity reconstruction and pose estimation,” in *Proc. of the Eur. Conf. on Comput. Vis.*, 2022, pp. 264–280.
- [27] M. Berman, K. Myszkowski, H.-P. Seidel, and T. Ritschel, “X-fields: Implicit neural view-, light-and time-image interpolation,” *ACM Trans. on Graphics*, vol. 39, no. 6, pp. 1–15, 2020.
- [28] Y. Chen, S. Liu, and X. Wang, “Learning continuous image representation with local implicit image function,” in *IEEE/CVF Comput. Soc. Conf. Comput. Vis. Pattern Recognit.*, 2021, pp. 8628–8638.
- [29] L. Yariv, Y. Kasten, D. Moran, M. Galun, M. Atzmon, B. Ronen, and Y. Lipman, “Multiview neural surface reconstruction by disentangling geometry and appearance,” *Advances in Neural Inf. Process. Syst.*, vol. 33, pp. 2492–2502, 2020.
- [30] V. Sitzmann, M. Zollhöfer, and G. Wetzstein, “Scene representation networks: Continuous 3d-structure-aware neural scene representations,” in *Advances in Neural Inf. Process. Syst.*, vol. 32, 2019.
- [31] A. Pumarola, E. Corona, G. Pons-Moll, and F. Moreno-Noguer, “D-nerf: Neural radiance fields for dynamic scenes,” in *IEEE/CVF Comput. Soc. Conf. Comput. Vis. Pattern Recognit.*, 2021, pp. 10313–10322.
- [32] K. Park, U. Sinha, J. T. Barron, S. Bouaziz, D. B. Goldman, S. M. Seitz, and R. Martin-Brualla, “Deformable neural radiance fields,” *arXiv preprint*, 2020.
- [33] E. Treitsch, A. Tewari, V. Golyanik, M. Zollhöfer, C. Lassner, and C. Theobalt, “Non-rigid neural radiance fields: Reconstruction and novel view synthesis of a dynamic scene from monocular video,” in *IEEE/CVF Int. Conf. on Comput. Vis.*, 2021, pp. 12939–12950.
- [34] Y. Du, Y. Zhang, H.-X. Yu, J. B. Tenenbaum, and J. Wu, “Neural radiance flow for 4d view synthesis and video processing,” in *IEEE/CVF Int. Conf. on Comput. Vis.*, 2021, pp. 14304–14314.
- [35] W. Xian, J.-B. Huang, J. Kopf, and C. Kim, “Space-time neural irradiance fields for free-viewpoint video,” in *IEEE/CVF Comput. Soc. Conf. Comput. Vis. Pattern Recognit.*, 2021, pp. 9421–9431.
- [36] X. Gao, S. Jin, C.-K. Wen, and G. Y. Li, “ComNet: Combination of deep learning and expert knowledge in OFDM receivers,” *IEEE Commun. Lett.*, vol. 22, no. 12, pp. 2627–2630, 2018.
- [37] M. Soltani, V. Pourahmadi, A. Mirzaei, and H. Sheikhzadeh, “Deep learning-based channel estimation,” *IEEE Commun. Lett.*, vol. 23, no. 4, pp. 652–655, 2019.
- [38] E. Balevi, A. Doshi, and J. G. Andrews, “Massive MIMO channel estimation with an untrained deep neural network,” *IEEE Trans. on Wireless Commun.*, vol. 19, no. 3, pp. 2079–2090, 2020.
- [39] A. Yu, V. Ye, M. Tancik, and A. Kanazawa, “pixelnerf: Neural radiance fields from one or few images,” in *IEEE/CVF Comput. Soc. Conf. Comput. Vis. Pattern Recognit.*, 2021, pp. 4576–4585.
- [40] L. Le Magoarou, T. Yassine, S. Paquelet, and M. Crussière, “Deep learning for location based beamforming with Nlos channels,” in *IEEE Int. Conf. on Acoust., Speech and Signal Process.*, 2022, pp. 8812–8816.
- [41] —, “Channel charting based beamforming,” in *2022 56th Asilomar Conf. Signals, Syst., Comput.*, 2022, pp. 1185–1189.
- [42] B. Chatelier, L. L. Magoarou, V. Corlay, and M. Criissière, “Model-based learning for location-to-channel mapping,” in *IEEE Int. Conf. on Acoust., Speech and Signal Process.*, 2024, pp. 12836–12840.
- [43] X. Zhao, Z. An, Q. Pan, and L. Yang, *NeRF2: Neural Radio-Frequency Radiance Fields*, 2023.
- [44] J. Hoydis, F. A. Aoudia, S. Cammerer, F. Euchner, M. Nimier-David, S. t. Brink, and A. Keller, “Learning radio environments by differentiable ray tracing,” *arXiv preprint*, Nov. 2023.
- [45] D. M. Pozar, *Microwave engineering*, Second ed. John Wiley & Sons, 1998.
- [46] D. Liu, K. Liu, Y. Ma, and J. Yu, “Joint TOA and DOA localization in indoor environment using virtual stations,” *IEEE Commun. Lett.*, vol. 18, no. 8, pp. 1423–1426, 2014.
- [47] V. Saragadam, D. LeJeune, J. Tan, G. Balakrishnan, A. Veeraraghavan, and R. G. Baraniuk, “Wire: Wavelet implicit neural representations,” in *IEEE/CVF Comput. Soc. Conf. Comput. Vis. Pattern Recognit.*, 2023, pp. 18507–18516.
- [48] D. Tse and P. Viswanath, *Fundamentals of Wireless Communication*. Cambridge University Press, 2005.
- [49] L. Le Magoarou, A. Le Calvez, and S. Paquelet, “Massive MIMO channel estimation taking into account spherical waves,” in *2019 IEEE 20th Int. Workshop on Signal Process. Advances in Wireless Commun. (SPAWC)*, 2019, pp. 1–5.
- [50] S. Mallat and Z. Zhang, “Matching pursuits with time-frequency dictionaries,” *IEEE Trans. Signal Process.*, vol. 41, no. 12, pp. 3397–3415, 1993.
- [51] Y. Pati, R. Rezaifar, and P. Krishnaprasad, “Orthogonal matching pursuit: recursive function approximation with applications to wavelet decomposition,” in *1993 27th Asilomar Conf. Signals, Syst., Comput.*, 1993, pp. 40–44 vol.1.
- [52] J. Schmidhuber, “Learning to control fast-weight memories: An alternative to dynamic recurrent networks,” *Neural Computation*, vol. 4, no. 1, pp. 131–139, 1992.
- [53] D. Ha, A. M. Dai, and Q. V. Le, “Hypernetworks,” in *Int. Conf. on Learn. Representations*, 2017.
- [54] J. Hoydis, S. Cammerer, F. Ait Aoudia, A. Vem, N. Binder, G. Marcus, and A. Keller, “Sionna: An open-source library for next-generation physical layer research,” *arXiv preprint*, 2022.

APPENDIX A PROOF OF LEMMA 1

Let $\mathbf{x}_r \in \mathbb{R}^3$ be a reference location and $\mathcal{D}_{\mathbf{x}} \subset \mathbb{R}^3$ be a local validity domain such that $\forall \mathbf{x} \in \mathcal{D}_{\mathbf{x}}, \|\mathbf{x} - \mathbf{x}_r\|_2 \leq \epsilon_{\mathbf{x}}$. The same holds true in the antenna subspace with the reference antenna location $\mathbf{a}_{l,r} \in \mathbb{R}^3$ and local validity domain $\mathcal{D}_{\mathbf{a}} \subset \mathbb{R}^3$ such that $\forall \mathbf{a}_{l,j} \in \mathcal{D}_{\mathbf{a}}, \|\mathbf{a}_{l,j} - \mathbf{a}_{l,r}\|_2 \leq \epsilon_{\mathbf{a}}$. Let $\xi(\mathbf{x}, \mathbf{a}_{l,j}) \triangleq \|\mathbf{x} - \mathbf{a}_{l,j}\|_2$. $\xi(\mathbf{x}, \mathbf{a}_{l,j})$ is differentiable at $\mathbf{x} = \mathbf{x}_r$. The first order Taylor expansion of $\xi(\mathbf{x}, \mathbf{a}_{l,j})$ around \mathbf{x}_r yields, $\forall \mathbf{x} \in \mathcal{D}_{\mathbf{x}}$:

$$\begin{aligned} \xi(\mathbf{x}, \mathbf{a}_{l,j}) &\simeq \xi(\mathbf{x}_r, \mathbf{a}_{l,j}) + \nabla_{\mathbf{x}} \|\mathbf{x} - \mathbf{a}_{l,j}\|_2 \Big|_{\mathbf{x}_r}^T (\mathbf{x} - \mathbf{x}_r) \\ &= \|\mathbf{x}_r - \mathbf{a}_{l,j}\|_2 + \frac{(\mathbf{x}_r - \mathbf{a}_{l,j})^T}{\|\mathbf{x}_r - \mathbf{a}_{l,j}\|_2} (\mathbf{x} - \mathbf{x}_r) \\ &= \|\mathbf{x}_r - \mathbf{a}_{l,j}\|_2 + \mathbf{u}_{l,j}(\mathbf{x}_r)^T (\mathbf{x} - \mathbf{x}_r). \end{aligned} \quad (23)$$

One has $\xi(\mathbf{x}_r, \mathbf{a}_{l,j}) = \|\mathbf{x}_r - \mathbf{a}_{l,j}\|_2$. $\xi(\mathbf{x}_r, \mathbf{a}_{l,j})$ is differentiable at $\mathbf{a}_{l,j} = \mathbf{a}_{l,r}$. As per the previous development, the first order Taylor expansion of $\xi(\mathbf{x}_r, \mathbf{a}_{l,j})$ around $\mathbf{a}_{l,r}$ yields, $\forall \mathbf{a}_{l,j} \in \mathcal{D}_{\mathbf{a}}$:

$$\xi(\mathbf{x}_r, \mathbf{a}_{l,j}) \simeq \|\mathbf{x}_r - \mathbf{a}_{l,r}\|_2 - \mathbf{u}_{l,r}(\mathbf{x}_r)^T (\mathbf{a}_{l,j} - \mathbf{a}_{l,r}). \quad (24)$$

Finally one has: $\forall (\mathbf{x}, \mathbf{a}_{l,j}) \in \mathcal{D}_{\mathbf{x}} \times \mathcal{D}_{\mathbf{a}} : \|\mathbf{x} - \mathbf{a}_{l,j}\|_2 \simeq \|\mathbf{x}_r - \mathbf{a}_{l,r}\|_2 + \mathbf{u}_{l,j}(\mathbf{x}_r)^T (\mathbf{x} - \mathbf{x}_r) - \mathbf{u}_{l,r}(\mathbf{x}_r)^T (\mathbf{a}_{l,j} - \mathbf{a}_{l,r})$.

APPENDIX B PROOF OF COROLLARY 1

Let $\mathbf{x}_r \in \mathbb{R}^3$ and $\mathbf{a}_{l,r} \in \mathbb{R}^3$ be a reference location and a reference antenna location respectively. Let $\Gamma_{\mathbf{x}_r} \triangleq (\mathbf{x}_r - \mathbf{a}_{l,j})(\mathbf{x}_r - \mathbf{a}_{l,j})^T$, and $\Gamma_{\mathbf{a}_r} \triangleq (\mathbf{a}_{l,r} - \mathbf{x}_r)(\mathbf{a}_{l,r} - \mathbf{x}_r)^T$. Let $\psi(\mathbf{x})$ be a double differentiable function at $\mathbf{x} = \mathbf{x}_r$. The second order of the Taylor expansion of $\psi(\mathbf{x})$ can be expressed as $e = \frac{1}{2}(\mathbf{x} - \mathbf{x}_r)^T \nabla_{\mathbf{x}} \nabla_{\mathbf{x}}^T \psi(\mathbf{x}) \Big|_{\mathbf{x}_r} (\mathbf{x} - \mathbf{x}_r)$. Letting $\psi(\mathbf{x}) = \|\mathbf{x} - \mathbf{a}_{l,j}\|_2$ and recalling that $\forall \mathbf{x} \in \mathbb{R}^3, \nabla_{\mathbf{x}} \nabla_{\mathbf{x}}^T \|\mathbf{x}\|_2 = \mathbf{Id}_2 / \|\mathbf{x}\|_2 - \mathbf{x}\mathbf{x}^T / \|\mathbf{x}\|_2^3$ yields:

$$\begin{aligned} e_1 &= \frac{1}{2} \left(\frac{\|\mathbf{x} - \mathbf{x}_r\|_2^2}{\|\mathbf{x}_r - \mathbf{a}_{l,j}\|_2} - \frac{(\mathbf{x} - \mathbf{x}_r)^T \Gamma_{\mathbf{x}_r} (\mathbf{x} - \mathbf{x}_r)}{\|\mathbf{x}_r - \mathbf{a}_{l,j}\|_2^3} \right) \\ &= \frac{1}{2} \left(\frac{\|\mathbf{x} - \mathbf{x}_r\|_2^2}{\|\mathbf{x}_r - \mathbf{a}_{l,j}\|_2} - o \left(\frac{1}{\|\mathbf{x}_r - \mathbf{a}_{l,j}\|_2^2} \right) \right), \end{aligned} \quad (25)$$

when $(\mathbf{x} - \mathbf{x}_r)^\top \mathbf{\Gamma}_{\mathbf{x}_r} (\mathbf{x} - \mathbf{x}_r) / \|\mathbf{x}_r - \mathbf{a}_{l,j}\|_2 \rightarrow 0$. The same approach applied to $\psi(\mathbf{a}_{l,j}) = \|\mathbf{a}_{l,j} - \mathbf{x}_r\|_2$ yields:

$$\begin{aligned} e_2 &= \frac{1}{2} \left(\frac{\|\mathbf{a}_{l,j} - \mathbf{a}_{l,r}\|_2^2}{\|\mathbf{x}_r - \mathbf{a}_{l,r}\|_2} - \frac{(\mathbf{a}_{l,j} - \mathbf{a}_{l,r})^\top \mathbf{\Gamma}_{\mathbf{a}_r} (\mathbf{a}_{l,j} - \mathbf{a}_{l,r})}{\|\mathbf{x}_r - \mathbf{a}_{l,r}\|_2^3} \right) \\ &= \frac{1}{2} \left(\frac{\|\mathbf{a}_{l,j} - \mathbf{a}_{l,r}\|_2^2}{\|\mathbf{x}_r - \mathbf{a}_{l,r}\|_2} - o\left(\frac{1}{\|\mathbf{x}_r - \mathbf{a}_{l,r}\|_2^2}\right) \right), \end{aligned} \quad (26)$$

when $(\mathbf{a}_{l,j} - \mathbf{a}_{l,r})^\top \mathbf{\Gamma}_{\mathbf{a}_r} (\mathbf{a}_{l,j} - \mathbf{a}_{l,r}) / \|\mathbf{x}_r - \mathbf{a}_{l,r}\|_2 \rightarrow 0$. Considering $e = e_1 + e_2$ concludes the proof.

APPENDIX C

PROOF OF PROPOSITION 1

Let $f_r \in \mathbb{R}$ such that $\forall f_k \in \mathbb{R}, f_k = (f_k - f_r) + f_r$. Eq. (4) can be rewritten as:

$$h_{j,k}(\mathbf{x}) = \sum_{l=1}^{L_p} \frac{\gamma_l}{\|\mathbf{x} - \mathbf{a}_{l,j}\|_2} e^{-j \frac{2\pi}{\lambda_r} \|\mathbf{x} - \mathbf{a}_{l,j}\|_2} e^{-j \frac{2\pi}{\lambda_{k-r}} \|\mathbf{x} - \mathbf{a}_{l,j}\|_2}, \quad (27)$$

where λ_r , resp. λ_{k-r} , is the wavelength associated to frequency f_r , resp. $f_k - f_r$. Let $\delta_{\mathbf{x}} \triangleq \mathbf{x} - \mathbf{x}_r$ and $\delta_{\mathbf{a}} \triangleq \mathbf{a}_{l,j} - \mathbf{a}_{l,r}$. Introducing Eq. (6) of Lemma 1 in Eq. (27) yields $\forall (\mathbf{x}, \mathbf{a}_{l,j}) \in \mathcal{D}_{\mathbf{x}} \times \mathcal{D}_{\mathbf{a}}$:

$$\begin{aligned} h_{j,k}(\mathbf{x}) &\simeq \sum_{l=1}^{L_p} \frac{\gamma_l}{\|\mathbf{x} - \mathbf{a}_{l,j}\|_2} e^{-j \frac{2\pi}{\lambda_{k-r}} \|\mathbf{x}_r - \mathbf{a}_{l,r}\|_2} \\ &\quad \cdot e^{-j \frac{2\pi}{\lambda_{k-r}} \mathbf{u}_{l,j}(\mathbf{x}_r)^\top \delta_{\mathbf{x}}} e^{j \frac{2\pi}{\lambda_{k-r}} \mathbf{u}_{l,r}(\mathbf{x}_r)^\top \delta_{\mathbf{a}}} \\ &\quad \cdot e^{-j \frac{2\pi}{\lambda_r} \|\mathbf{x}_r - \mathbf{a}_{l,r}\|_2} e^{-j \frac{2\pi}{\lambda_r} \mathbf{u}_{l,j}(\mathbf{x}_r)^\top \delta_{\mathbf{x}}} \\ &\quad \cdot e^{j \frac{2\pi}{\lambda_r} \mathbf{u}_{l,r}(\mathbf{x}_r)^\top \delta_{\mathbf{a}}}. \end{aligned} \quad (28)$$

Considering that the reference frequency f_r is on the same order than the current frequency f_k gives: $f_k - f_r \ll f_r \Rightarrow \lambda_r / \lambda_{k-r} \ll 1$. By definition of the validity domains, one has $\forall \mathbf{a}_{l,j} \in \mathcal{D}_{\mathbf{a}}, \|\delta_{\mathbf{a}}\|_2 \leq \epsilon_{\mathbf{a}}$ and $\forall \mathbf{x} \in \mathcal{D}_{\mathbf{x}}, \|\delta_{\mathbf{x}}\|_2 \leq \epsilon_{\mathbf{x}}$. Thus, the location and antenna differences $\delta_{\mathbf{a}}$ and $\delta_{\mathbf{x}}$ can be expressed as a small number of the reference wavelength in both directions, i.e. $\exists (\mathbf{m}_{\mathbf{a}}, \mathbf{m}_{\mathbf{x}}) \in \mathbb{R}^3 \times \mathbb{R}^3$ st. $\delta_{\mathbf{a}} \simeq \mathbf{m}_{\mathbf{a}} \lambda_r$, $\delta_{\mathbf{x}} \simeq \mathbf{m}_{\mathbf{x}} \lambda_r$ with $\|\mathbf{m}_{\mathbf{a}}\|_2$ and $\|\mathbf{m}_{\mathbf{x}}\|_2$ small. Then, $\forall (\mathbf{x}, \mathbf{a}_{l,j}) \in \mathcal{D}_{\mathbf{x}} \times \mathcal{D}_{\mathbf{a}}$:

$$\begin{cases} \delta_{\mathbf{a}} \simeq \mathbf{m}_{\mathbf{a}} \lambda_r \\ \delta_{\mathbf{x}} \simeq \mathbf{m}_{\mathbf{x}} \lambda_r \end{cases} \Rightarrow \begin{cases} \left| \frac{\mathbf{u}_{l,r}(\mathbf{x}_r)^\top \delta_{\mathbf{a}}}{\lambda_{k-r}} \right| \ll 1 \\ \left| \frac{\mathbf{u}_{l,j}(\mathbf{x}_r)^\top \delta_{\mathbf{x}}}{\lambda_{k-r}} \right| \ll 1 \end{cases}. \quad (29)$$

Furthermore, as in classical communication systems the inter-antenna spacing is on the order of the wavelength, one can use the following approximation: $\forall \mathbf{x}_r \in \mathbb{R}^3, \mathbf{u}_{l,j}(\mathbf{x}_r) \simeq \mathbf{u}_{l,r}(\mathbf{x}_r)$. Namely that the DoD towards the reference location \mathbf{x}_r , for each antenna, can be approximated as the DoD of the reference antenna. The limitations of this approximation are discussed in this paper. Introducing $d_{l,r} \triangleq \|\mathbf{x}_r - \mathbf{a}_{l,r}\|_2$, one then obtain, $\forall (\mathbf{x}, \mathbf{a}_{l,j}) \in \mathcal{D}_{\mathbf{x}} \times \mathcal{D}_{\mathbf{a}}$:

$$\begin{aligned} h_{j,k}(\mathbf{x}) &\simeq \sum_{l=1}^{L_p} \frac{\gamma_l}{\|\mathbf{x} - \mathbf{a}_{l,j}\|_2} e^{-j \frac{2\pi}{\lambda_r} d_{l,r}} e^{-j \frac{2\pi}{\lambda_r} \mathbf{u}_{l,r}(\mathbf{x}_r)^\top \delta_{\mathbf{x}}} \\ &\quad \cdot e^{-j \frac{2\pi}{\lambda_{k-r}} d_{l,r}} e^{j \frac{2\pi}{\lambda_r} \mathbf{u}_{l,r}(\mathbf{x}_r)^\top \delta_{\mathbf{a}}}. \end{aligned} \quad (30)$$

Additionally, as $\|\mathbf{x} - \mathbf{a}_{l,j}\|_2$ is a slowly varying term, one can approximate it as $d_{l,r}$ without suffering from a significant approximation error. One can then simplify the first two terms of Eq. (30) as $h_{l,r}(\mathbf{x}_r) \triangleq e^{-j \frac{2\pi}{\lambda_r} d_{l,r}} / d_{l,r}$. Finally, letting $\tau_{l,r} \triangleq d_{l,r} / c$ yields $2\pi d_{l,r} / \lambda_{k-r} = 2\pi (f_k - f_r) \tau_{l,r}$. One finally obtains: $\forall (\mathbf{x}, \mathbf{a}_{l,j}) \in \mathcal{D}_{\mathbf{x}} \times \mathcal{D}_{\mathbf{a}}$:

$$\begin{aligned} h_{j,k}(\mathbf{x}) &\simeq \sum_{l=1}^{L_p} \gamma_l h_{l,r}(\mathbf{x}_r) e^{-j \frac{2\pi}{\lambda_r} \mathbf{u}_{l,r}(\mathbf{x}_r)^\top (\mathbf{x} - \mathbf{x}_r)} \\ &\quad \cdot e^{-j 2\pi (f_k - f_r) \tau_{l,r}} e^{j \frac{2\pi}{\lambda_r} \mathbf{u}_{l,r}(\mathbf{x}_r)^\top (\mathbf{a}_{l,j} - \mathbf{a}_{l,r})}. \end{aligned} \quad (31)$$

APPENDIX D

PROOF OF THEOREM 1

Let us consider the tiling of the location subset $\mathcal{S}_{\mathbf{x}} \subset \mathbb{R}^3$ into $\Omega_{\mathbf{x}}$ location validity domains $\mathcal{D}_{\mathbf{x},i}$ with the Voronoi region of any given lattice. Note that for any subset of \mathbb{R}^3 , the optimal lattice is the D_3 -lattice. The same approach is applied for the antenna location subset $\mathcal{S}_{\mathbf{a}} \subset \mathbb{R}^3$, yielding $\Omega_{\mathbf{a}}$ local validity domains $\mathcal{D}_{\mathbf{a},i}$. By definition of the local validity domains and of the Taylor expansion, one has, $\forall (\mathcal{D}_{\mathbf{x},i}, \mathcal{D}_{\mathbf{a},i})$:

$$\forall (\mathbf{x}, \mathbf{a}_{l,j}) \in \mathcal{D}_{\mathbf{x},i} \times \mathcal{D}_{\mathbf{a},i}, \left\| \mathbf{H}(\mathbf{x}) - \hat{\mathbf{H}}(\mathbf{x}) \right\|_F < \epsilon, \quad (32)$$

where $\hat{\mathbf{H}}(\mathbf{x})$ is the Taylor-approximated channel matrix computed using Eq. (10). For each local validity domain $(\mathcal{D}_{\mathbf{x},i}, \mathcal{D}_{\mathbf{a},i})$ pair, Eq. (10) shows that the channel can be approximated using only L_p planar wavefronts, SVs, and FRVs. Thus, one can construct a dictionary of planar wavefronts $\psi_{\mathbf{x}} \in \mathbb{C}^D$, a dictionary of SVs $\Psi_{\mathbf{a}} \in \mathbb{C}^{N_a \times D}$, and a dictionary of FRVs $\Psi_{\mathbf{f}} \in \mathbb{C}^{N_s \times D}$ containing the needed atoms for every local validity domain pair. This yields $D \leq L_p \Omega_{\mathbf{x}} \Omega_{\mathbf{a}}$.

While the FRV dictionary atoms follow Eq. (12), the SV dictionary atoms can't be constituted from Eq. (11), as only the true antenna locations $\mathbf{a}_{1,j}$ are known. However, every virtual antenna can be rewritten as a translated and rotated version of its physical counterpart, i.e. $\forall l \neq 1, \exists! (\epsilon, \mathbf{R}_{\theta}) \in \mathbb{R}^3 \times \mathbb{R}^{3 \times 3}$, s.t. $\mathbf{a}_{l,j} = \mathbf{R}_{\theta} \mathbf{a}_{1,j} + \epsilon$. One then obtains:

$$\begin{aligned} (\mathbf{a}_{l,j} - \mathbf{a}_{l,r}) &= \mathbf{R}_{\theta} \mathbf{a}_{1,j} + \epsilon - \mathbf{R}_{\theta} \mathbf{a}_{1,r} - \epsilon \\ &= \mathbf{R}_{\theta} (\mathbf{a}_{1,j} - \mathbf{a}_{1,r}). \end{aligned} \quad (33)$$

While the antenna difference is not impacted by translations, it is impacted by rotations. However, one can easily show that the projection term in the SV is rotation equivariant:

$$\begin{aligned} \mathbf{u}_{l,r}(\mathbf{x}_r)^\top (\mathbf{a}_{l,j} - \mathbf{a}_{l,r}) &= \mathbf{u}_{l,r}(\mathbf{x}_r)^\top \mathbf{R}_{\theta} (\mathbf{a}_{1,j} - \mathbf{a}_{1,r}) \\ &= (\mathbf{R}_{\theta}^\top \mathbf{u}_{l,r}(\mathbf{x}_r))^\top (\mathbf{a}_{1,j} - \mathbf{a}_{1,r}) \\ &= \tilde{\mathbf{u}}_{l,r}(\mathbf{x}_r)^\top (\mathbf{a}_{1,j} - \mathbf{a}_{1,r}). \end{aligned} \quad (34)$$

Thus, the dictionary of SVs can be constructed using DoDs $\tilde{\mathbf{u}}_i \in \mathbb{R}^3$ and the true antenna location difference $(\mathbf{a}_{1,j} - \mathbf{a}_{1,r})$. Using the previously defined dictionaries and introducing an activation vector $\mathbf{w}(\mathbf{x}) \in \mathbb{C}^D$ to select the needed L_p atoms at the current location \mathbf{x} , such that $\varpi(\mathbf{x}) = \mathbf{w}(\mathbf{x}) \odot \psi_{\mathbf{x}}(\mathbf{x})$, yields Eq. (16) and concludes the proof.